

Synthesis of organic-inorganic hybrid nanoparticles and their application in additive manufacturing

The thesis presented to the Faculty of the Graduate School of Cornell University
In Partial Fulfillment of the Requirements for the Degree of
Master of Science

by
Dung-Yi Wu
August 2019

© 2019 Dung-Yi Wu

TABLE OF CONTENTS

1. ABSTRACT.....	1
2. INTRODUCTION.....	3
3. BIOGRAPHICAL SKETCH.....	15
4. ACKNOWLEDGMENTS.....	17
5. REFERENCES.....	18
6. CHAPTER 1. MINI-EMULSION ARGET-ATRP FOR THE SYNTHESIS OF SILICA-POLY(METHYL METHACRYLATE) HAIRY NANOPARTICLES	26
6.1. Abstract	26
6.2. Introduction	27
6.3. Methods.....	29
6.3.1. Materials	29
6.3.2. Synthesis of 11-(ethoxydimethylsilyl)undecyl 2-bromo-2-methylpropanoate.....	29
6.3.3. Pre-treatment of Ludox-TM40 particles.....	30
6.3.4. Preparation of EDMP-functionalized Ludox TM-40 nanoparticles	31
6.3.5. Synthesis of silica-poly(methyl methacrylate) hairy nanoparticles.....	31
6.3.6. Instruments.....	32
6.4. Results and Discussion.....	33
6.5. Conclusion.....	40
6.6. Acknowledgments.....	41
6.7. Supporting Information	42
6.8. References.....	48
7. CHAPTER 2. THREE DIMENSIONAL PRINTING OF ZINC-OXIDE NANOSTRUCTURES FOR MULTIFUNCTIONAL APPLICATIONS.....	50
7.1. Abstract	50
7.2. Introduction	51
7.3. Methods.....	53
5.3.1 Materials	53
7.3.2. Synthesis and patterning of ZnO-MAA NPs.....	53
7.3.3. Fabrication of 3D printed amorphous ZnO film.....	54

7.3.4.	Preparation of TEM samples	54
7.3.5.	Instruments.....	54
7.3.6.	Transmission line measurement.....	55
7.4.	Results and Discussion.....	56
7.4.1.	Dispersion and characterization of ZnO-MAA NPs.....	56
7.4.2.	Film properties of 3D printed ZnO layer	59
7.4.3.	Optical projection of 3D structures.....	62
7.4.4.	Electrical properties of 3D printed ZnO	63
7.5.	Conclusion.....	66
7.6.	Acknowledgments.....	67
7.7.	Supporting Information	68
7.8.	References	74
8.	SUMMARY AND OUTLOOK.....	79

1. ABSTRACT

In recent years, organic-inorganic hybrid nanoparticles (OIHNs) have caught the attention of both academia and industry since well-established classes of materials, such as metals, polymers, and ceramics, maybe limited in their properties. These traditional materials cannot satisfy the requirements needed for many novel applications, such as sensor biohybrid materials, and photonic devices. OIHNs, on the other hand, have properties unique to inorganic nanoparticles, such as chemical resistivity, as well as the easy processability of organic materials. For example, OIHNs created in our group by integrating organic ligands with low extreme ultraviolet (EUV) radiation absorption, together with high-absorption metal-oxide nanoparticles, such as ZrO_2 and HfO_2 , may be useful as a future material for EUV lithography.

Chapter 1 focuses on the synthesis of hairy nanoparticles (HNPs). Specifically, silica-poly(methyl methacrylate) (SiO_2 -PMMA) nanoparticles were synthesized using an Activator Regenerated by Electron Transfer - Atomic Transfer Radical Polymerization (ARGET-ATRP) in mini-emulsion. The influence of Sample parameters such as MMA concentration and MMA feeding rate, as well as the roles of acetone and tetra-n-butylammonium bromide (TBAB) on the brush canopy size, graft density, M_n of the grafted polymer chains, and Sample kinetics, were investigated. In the future, the resulting, well-defined HNPs may serve as important building blocks in the creation of functional superlattices by tailoring polymer entanglement and interactions between HNPs.

Chapter 2 highlights a specific application of OIHNs. The surfaces of zinc oxide nanoparticles were modified with photosensitive ligands for the purpose of three-dimensional (3D) printing. These zinc oxide nanoparticles were used as nano-building blocks to enable the fabrication of complex, arbitrary 3D geometries at room temperature using Digital Light Processing (DLP) stereolithography, with a resolution approaching 50 μm . Moreover, the electronic properties of the 3D metal oxide structure remaining after calcination were studied

ABSTRACT

by transmission line measurement. These proof-of-concept results open up a broad opportunity space for 3D printing zinc oxide mesostructures in applications such as optoelectronics.

2. INTRODUCTION

Over recent years, organic-inorganic hybrid nanoparticles (OIHNs) have caught the attention in both academia and industry since well-established classical materials, such as metals, polymers, and ceramic, cannot satisfy all requirements needed for innovative applications, such as biohybrid materials and photonic devices.¹ OIHNs, on the other hand, have unique properties of inorganic nanoparticle, such as mechanical properties, thermal stability, as well as chemical functionalities of the organic component. The surface modification enables better integration between inorganic nanoparticle and organic material, which enhances OIHNs' thermal stability, chemical resistivity, mechanical properties, biocompatibility, optical properties, and electrical properties.²⁻⁴

For instance, Jain *et al.*⁵ made use of Au OIHNs, which possessed localized surface plasmon resonance properties, for diseases diagnosis and molecular imaging. Murray *et al.*⁶ created three-dimensional (3D) superstructures from size-tunable semiconductor quantum dots (e.g. CdSe, PbSe), which had fluorescent property.

Hairy nanoparticles (HNPs) is one class of OIHNs, which can serve as building blocks for the preparation of 2D arrays and 3D superlattices. In literature, different HNP synthesis methods had been investigated, including surface initiated living anionic polymerization (SILAP), reversible addition fragmentation chain transfer polymerization (RAFT), atom transfer radical polymerization (ATRP), and nitroxide mediated polymerization (NMP). Some examples were discussed as follows.

(a) Surface Initiated Living Anionic Polymerization (SILAP)

One successful example is from Zhou *et al.*, who grafted styrene on the surface of silica particles using SILAP. The initiator, 1,1-diphenylethylene, was initially functionalized with alkyldimethylchlorosilane, and attached to the silica surface. Then, n-BuLi was used as the activator for this reaction.⁷ Eike Hubner *et al.*⁸ modified the silica surface with multifunctional chlorosilanes and polymers, synthesized previously using anionic polymerization, were grafted to the silica surface. The graft density of these HNPs was around 1 chain/nm² with a narrow polydispersity. The disadvantage of SILAP is the sensitivity to carbon dioxide, water, and impurities.⁹ Therefore, more groups have moved on to controlled polymerization process that is more user-friendly, such as RAFT, NMP, ATRP.

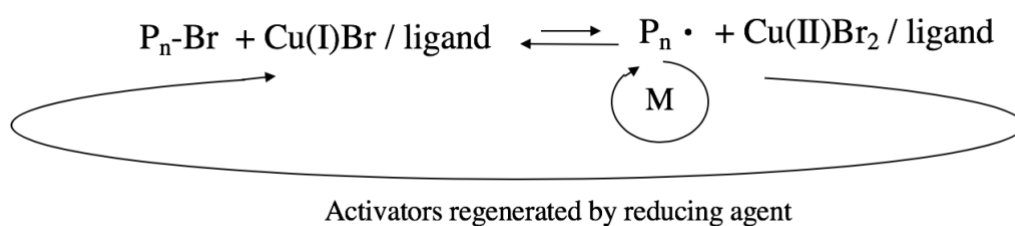
A review for the synthesis of different HNP structures using RAFT was reported by Stenzel *et al.* with different grafting methods.¹⁰ Kutcherlapati *et al.*¹¹ synthesized silica nanoparticles modified with glycopolymer by RAFT through “grafting from” technique. Varied molecule weights of glycopolymer chains were obtained. The polymer chains of these HNPs had narrow polydispersity index with a size range of 50-60 nm. Li *et al.*¹² made magnetic Fe₃O₄ nanoparticles grafted with chiral polymer brushes (p-[(1-methyl-2,2-dimethyl-5-oxo-4-imidazolidinyl)methyl]phenyl methacrylate), which had well-defined molecular weight by RAFT. These well-synthesized HNPs can effectively catalyze the asymmetric Diels–Alder reaction.

NMP is a method that has been widely applied to the preparation of novel polymer architectures. NMP possesses many advantages, such as high monomer compatibility, simplicity, and polymer purity.¹³ One example was shown by Bartholome *et al.*,¹³ who attached polystyrene on triethoxysilyl-terminated alkoxyamine functionalized silica. The surface of silica particles was covered with 40% alkoxyamine initiator. After NMP, the graft density of these HNPs was around 110 chains per particle. Sill *et al.*¹⁴ grew polystyrene and poly(styrene-*r*-methyl methacrylate) copolymers on CdSe cores. These surface modified HNPs enhanced the inherent fluorescence property of CdSe cores.

(d) Atom-Transfer Radical Polymerization (ATRP)

One interesting example is from Qin *et al.*,¹⁵ who made magnetic hybrid nanoparticles by grafting glycidyl methacrylate on silica coated Fe₃O₄ cores to improve the accuracy of protein quantification. Li *et al.*¹⁶ attached thermosensitive polymer brushes on silica nanoparticles by ATRP and studied the thermal-induced transition of these HNPs in water. Ohno *et al.*¹⁷ synthesized monodisperse silica HNPs with diameters ranging from 100 and 1500 nm. The surface was modified by MMA in a water solution. Although traditional ATRP has many advantages, a considerable amount of transition metal complex used in the reaction would cause damage to the environment. Therefore, in the past few years, researchers have made efforts to decrease the metal complex concentration. For instance, Krzysztof Matyjaszewski *et al.*¹⁸ reduced the metal complex concentration to 50 ppm, but still successfully synthesized well-defined poly(*n*-butyl acrylate). To improve the efficiency of ATRP, Matyjaszewski *et al.*^{19, 20} introduced the reducing agents, such as tin(II) 2-ethylhexanoate (Sn(EH)₂) and glucose, to ATRP system. These reducing agents regenerate Cu(I) species, which is the ATRP activator, from Cu(II) species without producing new initiating species. This method is called

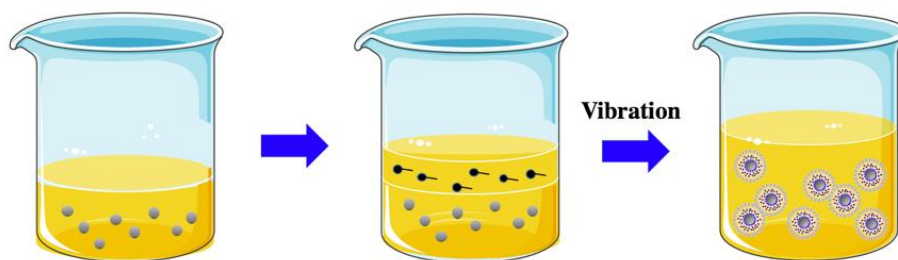
activator regenerated by electron transfer (ARGET)-ATRP (Scheme 1). ARGET-ATRP reduces the amount of metal complex used in the reaction and has better control over the molecular weight and polydispersity of polymer chains with much higher conversion. This green procedure is appropriate for industrial HNP scale up production. However, the selection of reducing agent is vital; otherwise, side reactions might occur among bad reducing agent, oxidized metal complex and reagents, which would lead to uncontrollable polymerization.



Scheme 1. Chemical equation of ARGET-ATRP. By introducing the reducing agent, the activator, Cu(I), can be regenerated from the deactivator, Cu(II).

(e) Mini-Emulsion Polymerization

Emulsion polymerization is a technique commonly used to make monodisperse particles. Ugelstad *et al.*²¹ synthesized polystyrene and polydivinylbenzene particles, which had a uniform size around 50 μm . Mini-emulsion polymerization is one category of emulsion polymerization for making smaller scales nanoparticles. One interesting example is from Jing Hu *et al.*²² The monomer oil droplets were well-dispersed in the nanoscale (50nm-1 μm) by external strength, such as sonication. Radicals were generated in the aqueous phase and transferred into monomer-swollen micelles to form nanoparticles (Scheme 2). The polymerization was localized in micelles. Therefore, the particles size can be well-controlled. Water-based polymerizations have many benefits such as environmentally friendly and easy to work with, especially in large scale HNP production.



Scheme 2. The mini-emulsion polymerization process for the preparation of nanoparticles.

The characteristics of HNPs are closely related to the graft density of the organic canopy, σ (Figure 1). Polymers grafted on inorganic particles have different conformations under varied graft densities. Low graft density shows “mushroom-like” conformation. As the graft density increases, the chains are forced to extend into a semi-dilute polymer brush (SDPB), and then to a concentrated polymer brush (CPB) conformation. At low grafting density, the radius of gyration for polymeric chains, R_g , is smaller so the neighboring chains would not interact with each other. In this regime, the polymeric chains adjust themselves to a mushroom-like conformation on the surface. When the height of polymer chains extended to approximately $h \approx 2R_g$, the polymer chains reach to the SDPB area.²³ Farnandes *et al.*²⁴ calculated the relation of chain height to degree of polymerization in SDPB (curved brushes) region using equation 1:

$$h \propto l_0 N \sigma^{*1/3} \quad (\text{Equation 1})$$

h refers to the height of the chain. l_0 is the monomer length. N is the polymerization degree. $\sigma^* = \sigma l_0^2$ is the reduced grafting density.

As the grafting density increases, the interactions between polymer chains become more important. At CPB (flat brushes) regime, we can calculate the relation of chain height to the degree of polymerization by equation 2:

$$h \propto l_0 N \sigma^{*1/2} \quad (\text{Equation 2})$$

Figure 1 shows the conformation of polymer brushes changes with the graft density. In CPB region, polymer chains form flatter brushes. Equation 3 determined the transition between SDPB and CPB:

$$R_c = R_0 \sigma^{*1/2} (\nu^*)^{-1} \quad (\text{Equation 3})$$

σ^* is the reduced graft density and ν^* is the excluded volume. For CPB region, $h + r_0 \leq r_c$.

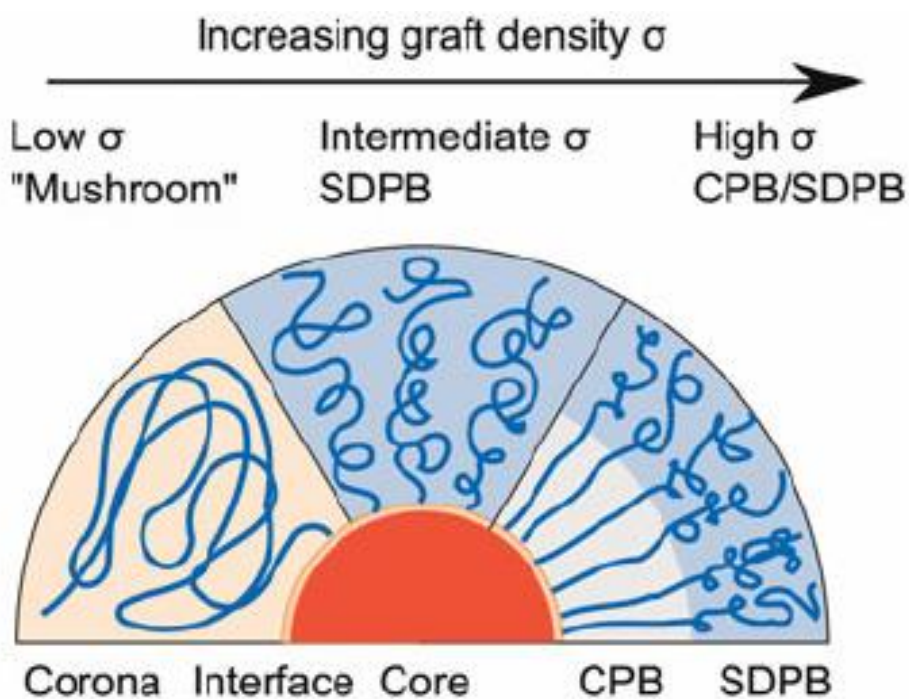


Figure 1. Low graft density shows “mushroom-like” conformation. As the graft density increases, the chains are forced to extend into a SDPB, and then into a CPB conformation.

When the graft density is in the SDPB region, polymer chains are more relaxed. These relaxed chains would further form polymer entanglement and result in HNP assemblies. The construction of HNP assemblies can be held up by van der waals forces, such as H-bonding, chain entanglement or by chemical bonds, such as crosslinking or click chemistry. Changing the interaction between HNPs can enhance their mechanical properties. For instance, Hansoge *et al.*²⁵ proofed that the graft density and the length of chains directly govern the mechanical properties of HNPs. Hansoge *et al.* grafted PMMA to nano-crystal nanoparticles to construct HNP assemblies. They found that the HNP assemblies reached the highest toughness and stiffness in the SDBP regime. JianingGao *et al.*²⁶ improved the fracture toughness and tensile modulus of polyhexylmethacrylate-b-polyglycidylmethacrylate-silica nanoparticles by lowering the HNP graft density to the SDBP.

HNPs can serve as building blocks to form functional materials, which have interesting optical, electronic, magnetic and biological properties associated with particle sizes and quantum effects.²⁷ These innovative functional materials are created by integrating neighboring particles. The organization is driven by self-assembly forces, such as polymer entanglement, and intermolecular interactions. Ohno *et al.*²⁸ synthesized Au nanoparticles with high graft density polymer brush and fabricated them to structural ordered metal assemblies. Akcora *et al.*²⁹ synthesized silica nanoparticles, which were grafted with different polymer brushes, such as poly(2-hydroxyethyl methacrylate), poly(3-sulfopropyl methacrylate) and poly(2-ethoxyethyl methacrylate). These silica HNPs assembled nanoporous membranes, which possessed interesting properties such as recyclability and retentate recovery. Yong *et al.*³⁰ synthesized Fe₃O₄ nanoparticles modified by glycidyl methacrylate and methacryloxyethyl trimethyl ammonium chloride for drug delivery. Yang *et al.*³¹ grafted ferroelectric polymer [poly(vinylidene fluoride-co-hexafluoro propylene)] on high dielectric constant nanoparticles

(BaTiO₃) for energy storage devices. Choudhury *et al.*³² synthesized poly(ethylene oxide) attached SiO₂ nanoparticles for lithium metal battery.

Previously, our group has successfully synthesized low polydispersity index ($\mathcal{D} < 1.2$) PMMA HNPs using a new aqueous ARGET-ATRP mini-emulsion polymerization method called mini monomer encapsulated emulsion polymerization. These size-controlled PMMA HNPs were presented in aqueous solution with acetone, tetrabutyl ammonium bromide (TBAB) and surfactant (Pluronic F-127). We also introduced this method to the synthesis of SiO₂-PMMA HNPs nanoparticles. Initially, the surface of LudoxTM-40 was functionalized by ATRP initiator and then ARGET-ATRP mini-emulsion polymerization was started. However, a considerable amount of ungrafted PMMA was produced during the reaction. In Chapter 1, this work aimed to reduce the formation of ungrafted PMMA and tune the grafting density, size of polymer canopy and polymer content of SiO₂-PMMAHNPs for a straightforward HNP synthesis.

Three Dimensional Printing

Additive manufacturing (AM), also known as three-dimensional (3D) fabrication, is an innovative technique that constructs 3D objects layer-by-layer deposition.³³⁻³⁵ Compared to traditional manufacturing techniques, 3D printing has significant advantages, such as the availability of a wide variety of materials, no requirement for molds, and the ability to create highly complex products.³⁶⁻³⁸ These advantages have boosted the development of 3D printing, and have caught both attention from academia and industry.^{38,39} In the past, 3D fabrication was only considered as a prototype technique due to its low printing speed. Now, large-scale manufacturing using innovative 3D printing techniques is doing away this stereotype.⁴⁰⁻⁴² This achievement has been reached by the improvement of 3D printing techniques including fused deposition modeling (FDM), stereolithography (SL), digital light processing (DLP), selective laser sintering (SLS) and binder jetting.

(a) Fused Deposition Modeling(FDM)

FDM is one of the most popular AM methods for printing thermoplastic materials with different functionalities. Some common materials that were proceeded by FDM were ABS, PC, and PLA. Furthermore, work has been done by blend inorganic components with these thermoplastics to expand the variability and applications.⁴³ Xu *et al.*⁴⁴ employed FDM to fabricate polycaprolactone/hydroxyapatite artificial bones. These bones showed good mechanical properties and biocompatibility, which can be applied to the treatment for patients with bone defects. Isakov *et al.*⁴⁵ 3D printed a polymer (e.g. acrylonitrile butadiene styrene, polypropylene) -based micro-ceramic (e.g. BaTiO₃ CaTiO₃) composite, which had varied dielectric permittivity, and high dielectric anisotropy.

(b) Stereolithography (SL)

So far, SL has been one promising method to process highly complicated and customized microstructure due to its flexibility and precision.^{46,47} SLA uses dot matrix laser light to sculpt images layer-by-layer in a very time-consuming manner. Cooke *et al.*⁴⁸ made biodegradable resins for stereolithography by mixing diethyl fumarate, poly(propylene fumarate), and a photo-initiator, bisacylphosphine oxide. This resin has been applied to tissue engineering for bony substrates. Lopes *et al.*⁴⁹ made silver SL resins to fabricate 3D structures, which embedded electronic circuits. This manufacturing process enables a direct and rapid 3D printing method for 3D packaging materials.

(c) Digital light Processing (DLP)

DLP is analogous to photolithography and is a resemble of SLA as they both create 3D structures using a photosensitizer to crosslink the matrix when exposed to UV light.⁵⁰⁻⁵² Structural information is transferred by black and white images layer-by-layer, once at a time to produce high-quality 3D products; DLP technique is more time-efficient and has lower manufacturing costs.⁵³ DLP is able to generate highly complex 3D architectures from nanoscale to mesoscale with sub-micrometer precision. Thrasher *et al.*⁵⁴ used silicones, hydrogels, and hybrids thereof as DLP resins, and the products displayed maximum elongations of up to 472% under tensile load.

(d) selective laser sintering (SLS)

SLS is well-known for its precise control over the microstructures, and it is also a prototyping process to fabricate 3D structures directly from ceramic and metal without blending organic components. During the process, bonding and sintering between neighboring

particles take place by raising the temperature above the melting point of the material using laser beams. The quality of the products is closely related to the energy of the laser beam, absorption of the material, surface tension and the particle size.⁵⁵ Olakanmi *et al.*⁵⁶ used SLS to print aluminum alloy 3D structures. This work provides a basis for future research on developing highly productive 3D printing technique for metals. Tan *et al.*⁵⁷ made temporary three-dimensional scaffolds, which were consisted of polyetheretherketone/hydroxyapatite composite, using commercial SLS system, for biological purpose.

(e) Binder Jetting

Binder jetting is an AM method, which liquid binder is dropped on the selected area of a powder bed. The binder will interact with powder particles and solidify to a form cross-sectional layer. Then, this layer will be lifted up by the stage. As the second layer is formed, it will be stitched onto the first layer. By printing out layer by layer, a 3D arbitrary structure can form. Bai *et al.*⁵⁸ made copper powders binder to fabricate high-purity copper structures, which has geometrically complex shapes. These copper products were applied to thermal management systems and structural electronics. Gonzalez *et al.*⁵⁹ fabricated aluminum oxide mesostructures. After 16 hours of the sintering process, the aluminum oxide mesostructures possessed an average compressive strength of 131.86 MPa, and a dielectric constant of 9.47–5.65 for a frequency range of 20 Hz to 1 MHz.

In chapter 2, we used DLP to fabricate arbitrary ZnO 3D structures. By modifying the ZnO surface by photosensitive ligands, methacrylic acid (MAA), programmable 3D structures were precisely constructed from nano- to macro-scale based on these building units. MAA ligands play a critical role in increasing colloidal stability. Two possible mechanisms might take place including ligand stripping, and free radical polymerization, which results in a

INTRODUCTI

solubility change that forms the pattern. Optical and scanning electron microscopy (SEM) images reveal that the printed samples have a good resolution (ca. 50 μm). Also, 3D printed ZnO tunnels show lower resistivity and rectifying behavior after calcined. This study suggests the possibility of using metal-oxide as DLP ink for future applications on semiconducting devices.

3. BIOGRAPHICAL SKETCH

Dung-Yi Wu was born in Kaohsiung, Taiwan. In May 2016, he graduated from the National Taiwan University of Science and Technology in Taipei, Taiwan with a B.Sc. in Materials Science and Engineering. During his undergraduate studies, he had the opportunity to work on the synthesis and characterization of novel biodegradable polymers with his thesis advisor and research mentor, Ming-Chien Yang. Under Prof. Yang, he gained experience with polymer processing, spectrometric identification, and biocompatibility analysis. During his final year of undergraduate studies, he independently worked on research leading to the publication of his article “Improvement of Cytocompatibility of Polylactide by Filling with Marine Algae Powder” in the *Journal of Materials Science & Engineering C - Materials for Biological Applications*, 50, 309-316. As a result of his research, he was awarded a fellowship by the Taiwan Ministry of Science and Technology in 2015-16.

Dung-Yi is particularly interested in the synthesis of novel materials for use in nanotechnology, so in September 2017 he began working towards his M.Sc. degree under the supervision of Prof. Christopher K. Ober and Prof. Tobias Hanrath in the department of Materials Science and Engineering at Cornell University. During this time, he participated in two research projects. For his first project, he synthesized SiO₂-PMMA hairy nanoparticles using ARGET-ATRP in a mini-emulsion system. The green methods he developed have great potential in the future large-scale synthesis of 2D arrays and 3D superlattice materials. For his second project, he developed a novel method for 3D printing complex electronic structures using zinc-oxide-based nanoparticles as building blocks. This process can be used to 3D print electronically conductive pathways, with a broad range of mesoscale applications in fields such as optoelectronics.

BIOGRAPHIC

Throughout his time at Cornell, he has benefitted from exposure to a broad range of scientific and engineering disciplines. After graduation, he will attend Johns Hopkins University to pursue his Ph.D.

4. ACKNOWLEDGMENTS

Without the undying support of my peers and mentors, I would not be where I am today. I would like to sincerely thank all those who have helped make my years at Cornell University both productive and memorable.

First and foremost, I would like to express my deepest gratitude to my advisor, Prof. Christopher K. Ober. From you, I developed an appreciation for developing materials on the smallest scales, for these will undoubtedly play the greatest role in our society's future. Under your mentorship, I grew immensely both as a scientist and as a person. Moreover, I received tremendous assistance from members of the Ober Group, especially Dr. Florian Käfer, Dr. Hong Xu, Dr. Roselynn Cordero, Nicholas Diaco, and Kou Yang.

I would also like to sincerely thank my co-advisor, Prof. Tobias Hanrath. You provided me with the direction and guidance I needed when my research was still in its infancy. Furthermore, your description of failure as the birthplace of science's greatest discoveries has influenced me deeply. I would also like to thank all the members of the Hanrath Group, Jen-Yu Huang in particular, for their technical support and helpful discussions.

This work was performed in part at the Cornell NanoScale Facility, a member of the National Nanotechnology Coordinated Infrastructure (NNCI), which is supported by the National Science Foundation (Grant ECCS-1542081). The project on the synthesis of SiO₂-PMMA HNPs made use of the Cornell Center for Materials Research (CCMR) Shared Facilities, which are supported through the NSF MRSEC program (DMR-1719875). I am grateful for the scientific and technical assistance from Cornell's Center for Nanomaterials Engineering and Technology.

Finally, I am so grateful to my family back home and to the new family I've become a part of at Cornell University. I will cherish our shared memories for the rest of my life.

5. REFERENCES

- (1) Mir, S. H.; Nagahara, L. A.; Thundat, T.; Mokarian-Tabari, P.; Furukawa, H.; Khosla, A. Review—Organic-Inorganic Hybrid Functional Materials: An Integrated Platform for Applied Technologies. *Journal of The Electrochemical Society* **2018**, 165 (8).
- (2). Skaff, H.; Emrick, T. Reversible Addition Fragmentation Chain Transfer (RAFT) Polymerization from Unprotected Cadmium Selenide Nanoparticles. *Angewandte Chemie* **2004**, 116 (40), 5497-5500.
- (3) Kumar, S. K.; Jouault, N.; Benicewicz, B.; Neely, T. Nanocomposites with Polymer Grafted Nanoparticles. *Macromolecules* **2013**, 46 (9).
- (4) Xu, F. J.; Kang, E. T.; Neoh, K. G. UV-Induced Coupling of 4-Vinylbenzyl Chloride on Hydrogen-Terminated Si(100) Surfaces for the Preparation of Well-Defined Polymer–Si Hybrids via Surface-Initiated ATRP. *Macromolecules* **2005**, 38 (5), 1573-1580.
- (5) Jain, P. K.; Huang, X.; El-Sayed, I. H.; El-Sayed, M. A. Noble metals on the nanoscale: optical and photothermal properties and some applications in imaging, sensing, biology, and medicine. *Acc Chem Res* **2008**, 41 (12), 1578-86.
- (6) Ermakov, V. A.; Silva Filho, J. M. C. d.; Bonato, L. G.; Mogili, N. V. V.; Montoro, F. E.; Iikawa, F.; Nogueira, A. F.; Cesar, C. L.; Jiménez-Villar, E.; Marques, F. C. Three-Dimensional Superlattice of PbS Quantum Dots in Flakes. *ACS Omega* **2018**, 3 (2), 2027-2032.
- (7) Zhou, Q.; Wang, S.; Fan, X.; Advincula, R. Living Anionic Surface-Initiated Polymerization (LASIP) of a Polymer on Silica Nanoparticles. *Langmuir* **2002**, 18, 3324-3331.
- (8) Hübner, E.; Allgaier, J. r.; Meyer, M.; Stellbrink, J. r.; Pyckhout-Hintzen, W.; Richter, D. Synthesis of Polymer/Silica Hybrid Nanoparticles Using Anionic Polymerization Techniques. *Macromolecules* **2010**, 43 (2), 856-867.

REFERENCES

- (9) Veerle M. C.; Coessens, C.; Matyjaszewski, K. Fundamentals of Atom Transfer Radical Polymerization. *Journal of Chemical Education* **2010**, 87 (9), 916-919.
- (10) Stenzel, M. H. Hairy Core-Shell Nanoparticles via RAFT: Where are the Opportunities and Where are the Problems and Challenges? *Macromol Rapid Commun* **2009**, 30 (19), 1603-24.
- (11) Kutcherlapati, S. N. R.; Koyilapu, R.; Boddu, U. M. R.; Datta, D.; Perali, R. S.; Swamy, M. J.; Jana, T. Glycopolymer-Grafted Nanoparticles: Synthesis Using RAFT Polymerization and Binding Study with Lectin. *Macromolecules* **2017**, 50 (18), 7309-7320.
- (12) Li, X.; Zhang, S.; Yang, B.; Lv, C.; Jia, X.; Hu, Z. Magnetic Fe₃O₄ nanoparticles supporting Macmillan with controlled shell structure as an efficient and reusable catalyst for asymmetric reaction. *RSC Advances* **2016**, 6 (89).
- (13) Grubbs, R. B. Nitroxide-Mediated Radical Polymerization: Limitations and Versatility. *Polymer Reviews* **2011**, 51 (2), 104-137.
- (14) Sill, K.; Emrick, T. Nitroxide-Mediated Radical Polymerization from CdSe Nanoparticles. *Chemistry of Materials* **2004**, 16 (7), 1240-1243.
- (15) Qin, W.; Song, Z.; Fan, C.; Zhang, W.; Cai, Y.; Zhang, Y.; Qian, X. Trypsin immobilization on hairy polymer chains hybrid magnetic nanoparticles for ultra fast, highly efficient proteome digestion, facile ¹⁸O labeling and absolute protein quantification. *Anal Chem* **2012**, 84 (7), 3138-44.
- (16) Li, D.; Jones, G. L.; Dunlap, J. R.; Hua, F.; Zhao, B. Thermosensitive Hairy Hybrid Nanoparticles Synthesized by Surface-Initiated Atom Transfer Radical Polymerization. *Langmuir* **2006**, 22 (7), 3344-3351.

REFERENCES

- (17) Ohno, K.; Morinaga, T.; Koh, K.; Tsujii, Y.; Fukuda, T. Synthesis of Monodisperse Silica Particles Coated with Well-Defined, High-Density Polymer Brushes by Surface-Initiated Atom Transfer Radical Polymerization. *Macromolecules* **2005**, 38 (6), 2137-2142.
- (18) Queffelec, J.; Gaynor, S.G.; Matyjaszewski, K. Optimization of Atom Transfer Radical Polymerization Using Cu(I)/Tris(2-(dimethylamino)ethyl)amine as a Catalyst. *Macromolecules* **2000**, 33, 8629-8639.
- (19) Tsarevsky, N.V.; Matyjaszewski, K. "Green" Atom Transfer Radical Polymerization: From Process Design to Preparation of Well-Defined Environmentally Friendly Polymeric Materials. *Chem. Rev.* **2007**, 107, 2270–2299.
- (20) Matyjaszewski, K.; Tsarevsky, N. V. Macromolecular engineering by atom transfer radical polymerization. *J Am Chem Soc* **2014**, 136 (18), 6513-33.
- (21) Ugelstad, J.; Mfutakamba, H.R.; Mork, P.C. Preparation and application of monodisperse polymer particles. *Journal of Polymer Science: Polymer Symposium* **1985**, 72, 225-240.
- (22) Hu, J.; Chen, M.; Wu, L. Organic-inorganic nanocomposites synthesized via miniemulsion polymerization. *Polym. Chem.* **2011**, 2 (4), 760-772.
- (23) Dukes, D.; Li, Y.; Lewis, S.; Benicewicz, B.; Schadler, L.; Kumar, S. K. Conformational Transitions of Spherical Polymer Brushes: Synthesis, Characterization, and Theory. *Macromolecules* **2010**, 43 (3), 1564-1570.
- (24) Fernandes, N. J.; Koerner, H.; Giannelis, E. P.; Vaia, R. A. Hairy nanoparticle assemblies as one-component functional polymer nanocomposites: opportunities and challenges. *MRS Communications* **2013**, 3 (01), 13-29.
- (25) Hansoge, N. K.; Huang, T.; Sinko, R.; Xia, W.; Chen, W.; Keten, S. Materials by Design for Stiff and Tough Hairy Nanoparticle Assemblies. *ACS Nano* **2018**, 12 (8), 7946-7958.

REFERENCES

- (26) Gao, J.; Li, J.; Benicewicz, B. C.; Zhao, S.; Hillborg, H.; Schadler, L. S. The Mechanical Properties of Epoxy Composites Filled with Rubbery Copolymer Grafted SiO₂. *Polymers* **2012**, 4 (1), 187-210.
- (27) Moffitt, M. G. Self-Assembly of Polymer Brush-Functionalized Inorganic Nanoparticles: From Hairy Balls to Smart Molecular Mimics. *The Journal of Physical Chemistry Letters* **2013**, 4 (21), 3654-3666.
- (28) Ohno, K.; Koh, K.; Tsujii, Y.; Fukuda, T. Fabrication of ordered arrays of gold nanoparticles coated with high-density polymer brushes. *Angew Chem Int Ed Engl* **2003**, 42 (24), 2751-4.
- (29) Akcora, P.; Liu, H.; Kumar, S. K.; Moll, J.; Li, Y.; Benicewicz, B. C.; Schadler, L. S.; Acehan, D.; Panagiotopoulos, A. Z.; Pryamitsyn, V.; Ganesan, V.; Ilavsky, J.; Thiyagarajan, P.; Colby, R. H.; Douglas, J. F. Anisotropic self-assembly of spherical polymer-grafted nanoparticles. *Nat Mater* **2009**, 8 (4), 354-9.
- (30) Yong, Y.; Bai, Y.; Li, Y.; Lin, L.; Cui, Y.; Xia, C. Preparation and application of polymer-grafted magnetic nanoparticles for lipase immobilization. *Journal of Magnetism and Magnetic Materials* **2008**, 320 (19), 2350-2355.
- (31) Yang, K.; Huang, X.; Huang, Y.; Xie, L.; Jiang, P. Fluoro-Polymer@BaTiO₃ Hybrid Nanoparticles Prepared via RAFT Polymerization: Toward Ferroelectric Polymer Nanocomposites with High Dielectric Constant and Low Dielectric Loss for Energy Storage Application. *Chemistry of Materials* **2013**, 25 (11), 2327-2338.
- (32) Choudhury, S.; Mangal, R.; Agrawal, A.; Archer, L. A. A highly reversible room-temperature lithium metal battery based on crosslinked hairy nanoparticles. *Nat Commun* **2015**, 6, 10101.

REFERENCES

- (33) Ligon, S. C.; Liska, R.; Stampfl, J.; Gurr, M.; Mulhaupt, R. Polymers for 3D Printing and Customized Additive Manufacturing. *Chem. Rev.* **2017**, 117(15), 10212–10290.
- (34) Lin, D.; Nian, Q.; Deng, B.; Jin, S.; Hu, Y.; Wang, W.; Cheng, G. J. Three-Dimensional Printing of Complex Structures: Man Made or Toward Nature? *ACS Nano* **2014**, 8 (10), 9710–9715.
- (35) Farahani, R. D.; Dubé, M.; Therriault, D. Three-Dimensional Printing of Multifunctional Nanocomposites: Manufacturing Techniques and Applications. *Adv. Mater.* **2016**, 28(28), 5794–5821.
- (36) Manzano, J. S.; Weinstein, Z. B.; Sadow, A. D.; Slowing, I. I. Direct 3D Printing of Catalytically Active Structures. *ACS Catal.* **2017**, 7(11), 7567–7577.
- (37) Wang, X.; Guo, Q.; Cai, X.; Zhou, S.; Kobe, B.; Yang, J. Initiator-Integrated 3D Printing Enables the Formation of Complex Metallic Architectures. *ACS Appl. Mater. Interfaces* **2014**, 6(4), 2583–2587.
- (38) Johnson, B. N.; Lancaster, K. Z.; Zhen, G.; He, J.; Gupta, M. K.; Kong, Y. L.; Engel, E. A.; Krick, K. D.; Ju, A.; Meng, F.; Enquist, L. W.; Jia, X.; McAlpine, M. C. 3D Printed Anatomical Nerve Regeneration Pathways. *Adv. Funct. Mater.* **2015**, 25(39), 6205–6217.
- (39) Hart, L. R.; Li, S.; Sturgess, C.; Wildman, R.; Jones, J. R.; Hayes, W. 3D Printing of Biocompatible Supramolecular Polymers and their Composites. *ACS Appl. Mater. Interfaces* **2016**, 8(5), 3115–3122.
- (40) Hu, L.; Jiang, G. 3D Printing Techniques in Environmental Science and Engineering Will Bring New Innovation. *Environ. Sci. Technol.* **2017**, 51(7), 3597–3599.
- (41) Guvendiren, M.; Molde, J.; Soares, R. M. D.; Kohn, J. Designing Biomaterials for 3D Printing. *ACS Biomater. Sci. Eng.* **2016**, 2(10), 1679–1693.

REFERENCES

- (42) Kreiger, M.; Pearce, J. M. Environmental Life Cycle Analysis of Distributed Three-Dimensional Printing and Conventional Manufacturing of Polymer Products. *ACS Sustainable Chem. Eng.* **2013**, 1(12), 1511–1519.
- (43) Dudek, P. FDM 3D Printing Technology in Manufacturing Composite Elements. *Archives of Metallurgy and Materials* **2013**, 58 (4), 1415-1418.
- (44) Xu, N.; Ye, X.; Wei, D.; Zhong, J.; Chen, Y.; Xu, G.; He, D. 3D artificial bones for bone repair prepared by computed tomography-guided fused deposition modeling for bone repair. *ACS Appl Mater Interfaces* **2014**, 6 (17), 14952-63.
- (45) Isakov, D. V.; Lei, Q.; Castles, F.; Stevens, C. J.; Grovenor, C. R. M.; Grant, P. S. 3D printed anisotropic dielectric composite with meta-material features. *Materials & Design* **2016**, 93, 423-430.
- (46) Credi, C.; Fiorese, A.; Tironi, M.; Bernasconi, R.; Magagnin, L.; Levi, M.; Turri, S. 3D Printing of Cantilever-Type Microstructures by Stereolithography of Ferromagnetic Photopolymers. *ACS Appl. Mater. Interfaces* **2016**, 8, 26332–26342.
- (47) Lade, R. K.; Jr.; Hippchen, E. J.; Macosko, C. W.; Francis, L. F. Dynamics of Capillary-Driven Flow in 3D Printed Open Microchannels. *Langmuir* **2017**, 33(12), 2949–2964.
- (48) Cooke, M.N.; Fisher, J.P.; Dean, D.; Rinnac, C.; Mikos A.G. Use of Stereolithography to Manufacture Critical-Sized 3D Biodegradable Scaffolds for Bone Ingrowth. *Appl Biomater.* **2002**, 65–69.
- (49) Joe Lopes, A.; MacDonald, E.; Wicker, R. B. Integrating stereolithography and direct print technologies for 3D structural electronics fabrication. *Rapid Prototyping Journal* **2012**, 18 (2), 129-143.

REFERENCES

- (50) Pawar, A. A.; Halivni, S.; Waiskopf, N.; Ben-Shahar, Y.; Soreni-Harari, M.; Bergbreiter, S.; Banin, U.; Magdassi, S. Rapid Three-Dimensional Printing in Water Using Semiconductor–Metal Hybrid Nanoparticles as Photoinitiators. *Nano Lett.* **2017**, 17(7), 4497–4501.
- (51) Mandon, C. A.; Blum, L. J.; Marquette, C. A. Adding Biomolecular Recognition Capability to 3D Printed Objects. *Anal. Chem.* **2016**, 88(21), 10767–10772.
- (52) Kong, Y. L.; Tamargo, I. A.; Kim, H.; Johnson, B. N.; Gupta, M. K.; Koh, T. W.; Chin, H. A.; Steingart, D. A.; Rand, B. P.; McAlpine, M. C. 3D Printed Quantum Dot Light-Emitting Diodes. *Nano Lett.* **2014**, 14(12), 7017–7023.
- (53) Moonen, P. F.; Yakimets, I.; Huskens J. Fabrication of Transistors on Flexible Substrates: from Mass-Printing to High-Resolution Alternative Lithography Strategies. *Adv. Mater.* **2012**, 24(41), 5526–5541.
- (54) Thrasher, C. J.; Schwartz, J. J.; Boydston, A. J. Modular Elastomer Photoresins for Digital Light Processing Additive Manufacturing. *ACS Appl. Mater. Interfaces* **2017**, 9(45), 39708–39716.
- (55) Agarwala, M.; Bourell, D.; Beaman, J.; Marcus, H.; Barlow, J. Direct selective laser sintering of metals. *Rapid Prototyping Journal* **1995**, 1 (1), 26-36.
- (56) Olakanmi, E. O.; Cochrane, R. F.; Dalgarno, K. W. A review on selective laser sintering/melting (SLS/SLM) of aluminium alloy powders: Processing, microstructure, and properties. *Progress in Materials Science* **2015**, 74, 401-477.
- (57) Tan, K. H.; Chua, C. K.; Leong, K. F.; Cheah, C. M.; Cheang, P.; Abu Bakar, M. S.; Cha, S. W. Scaffold development using selective laser sintering of polyetheretherketone–hydroxyapatite biocomposite blends. *Biomaterials* **2003**, 24 (18), 3115-3123.
- (58) Bai, Y.; Williams, C. B. An exploration of binder jetting of copper. *Rapid Prototyping Journal* **2015**, 21 (2), 177-185.

REFERENCES

- (59) Gonzalez, J. A.; Mireles, J.; Lin, Y.; Wicker, R. B. Characterization of ceramic components fabricated using binder jetting additive manufacturing technology. *Ceramics International* **2016**, 42 (9), 10559-10564.

6. CHAPTER 1. MINI-EMULSION ARGET-ATRP FOR THE SYNTHESIS OF SILICA-POLY(METHYL METHACRYLATE) HAIRY NANOPARTICLES

6.1. Abstract

SiO₂-PMMA hairy nanoparticles (HNPs) were synthesized using Activator Regenerated Electron Transfer – Atom Transfer Radical Polymerization (ARGET-ATRP) in an aqueous mini-emulsion. Initially, the surfaces of monodisperse 25 nm diameter silica nanoparticles were modified with a hydrophobic ATRP initiator. These modified, hydrophobic nanoparticles were then dispersed as micelles in the aqueous phase using Pluronic F-127 surfactant. Tetra-n-butylammonium bromide (TBAB) was used as a phase transfer agent to shuttle both the monomer and ATRP catalyst-complex into the micelles to localize the polymerization of PMMA on the particle surfaces. This synthetic route allows the canopy size, graft density, and molar mass of the grafted polymer chains to be controlled by simply changing the monomer feeding rate. In the future, the resulting, well-defined HNPs may serve as important building blocks in the creation of functional superlattices by tailoring the polymer entanglement and interactions between HNPs.

6.2. Introduction

In recent years, Organic-Inorganic Hybrid Nanoparticles (OIHNs) have caught the attention of both academia and industry since well-established classes of materials, such as metals, polymers, and ceramics, are limited in their properties. HNPs, in particular, are unique in their capacity to interact with neighboring HNPs via brush entanglement and interactions, enhancing their thermal, mechanical and electrical properties in comparison to their single-component counterparts.¹ HNPs can serve as nano-building blocks for future applications such as sensors, biohybrid materials, and photonic devices.²⁻³ Nevertheless, several challenges still remain, limiting the straightforward synthesis of HNPs at multi-gram scales. Challenges include a complex purification procedure, in addition to the control of particle size, brush molecular weight, graft density, and particle aggregation.

Atomic Transfer Radical Polymerization (ATRP) is one of the most common and versatile methods for creating well-defined polymeric structures.⁴⁻⁵ For example, Pyun *et al.*⁶ synthesized PMMA- and PS-grafted silica HNPs using ATRP with nanoparticles dispersed in methyl isobutyl ketone. However, the use of organic solvents and large quantities of metal catalyst in traditional ATRP makes the purification procedure elaborate. To reduce the amount of copper catalyst used in the Sample, Matyjaszewski *et al.*⁷ introduced the ARGET-ATRP method by adding reducing agents to regenerate Cu(I) from Cu(II) during the Sample. Further, Matyjaszewski *et al.*⁸ demonstrated the synthesis of PS with a low $\bar{D}=1.17$ using parts-per-million concentrations of copper catalyst in environmentally friendly media (e.g., water).

The use of water-based polymerization would be beneficial for the direct, green synthesis of HNPs.⁹ Previous efforts have made use of ARGET-ATRP in emulsion as a scalable method for the synthesis of HNPs.¹⁰ One benefit of carrying out ATRP in emulsion is that the polymer

chain-end functionalities are preserved, which simplifies chain extension and particle surface modification. For instance, Min *et al.*¹¹ created a two-step, one-pot synthesis via emulsion methods for polymer-core HNPs. First, uniform nanogels consisting of MMA and ethylene glycol dimethacrylate were synthesized by ATRP in aqueous emulsion. Then, a second monomer, n-butyl acrylate, was grafted from initiating sites on the nanogel surfaces to form HNPs with well-controlled graft density and size. Similarly, Goel *et al.*¹² synthesized HNPs with silica cores by grafting poly(n-butyl acrylate)-*b*-PMMA block copolymers using mini-emulsion ARGET-ATRP in diphenylethylene. These HNPs possessed high graft density and a uniform particle size of around 15 nm. Notably, this work provides a feasible method for carrying out HNP production at industrial scale, in particular by reducing metal catalyst waste, giving more control over the polymer molecular weight, and yielding higher conversions than traditional ATRP. Nevertheless, none of these methods provide a straightforward method for the aqueous synthesis of HNPs with a metal-oxide core, which is the aim of this work.

Herein, we report the application of mini-emulsion ARGET-ATRP to generate well-defined SiO₂-PMMA HNPs. The monodisperse silica nanoparticles of 25 nm diameter were surface-modified with a hydrophobic ATRP initiator, suspended in surfactant-stabilized micelles in the aqueous phase, then grafted with PMMA. This work demonstrates that the brush canopy size, graft density, and chain molecular weight can be controlled by changing the MMA feeding rate. This method enables a straightforward synthesis for HNPs in aqueous solution, which has the potential to be applied to large-scale HNP production.

6.3. Methods

6.3.1. Materials

Copper (II) bromide (99%, extra pure, anhydrous), MMA (stabilized), L (+)-ascorbic acid, tetrabutylammonium bromide (99%), aluminum oxide (basic), and dimethylethoxysilane (94 wt%) were purchased from Acros Organics and used as received. Triethylamine, 2-bromoisobutyryl bromide (BIBB), Karstedt's catalyst in water, Pluronic F-127, 28% NH₃, and Ludox TM-40 particles were purchased from Sigma-Aldrich and used as received. Tris(2-pyridyl methyl) amine (TPMA, 98 wt%), was purchased from TCI. Ammonium hydroxide (28 wt%), hydrochloric acid (36.5-38.0 wt%), Dowex 50W X8 100-200 mesh, Dowex 1X8-200 mesh ion-exchange resin, and 10k MW cut-off 35 mm Snakeskin dialysis tubing were purchased from Fisher Chemical. The deionized water used in all experiments was obtained from a MilliporeSigma Milli-Q IQ 7000 Ultrapure Water System with a resistance of 18.2 MW.

6.3.2. Synthesis of 11-(ethoxydimethylsilyl)undecyl 2-bromo-2-methylpropanoate

The synthesis of the hydrophobic ATRP initiator, 11-(ethoxydimethylsilyl)undecyl 2-bromo-2-methylpropanoate (EDMP), was carried out in two steps (Scheme S1). Step 1 (bromination): 10-undecen-1-ol (4.257 g, 25 mmol) and pyridine (2.1 mL, 26 mmol) were dissolved in 30 mL of anhydrous tetrahydrofuran (THF) in a 100 mL round-bottom flask. 2-bromoisobutyryl bromide (BIBB) (5.760 g, 24 mmol, in 10 mL THF) was added dropwise over 2 hours, stirring the Sample at 0 °C in an ice bath. After 2 hours the ice bath was removed and the solution was subsequently stirred for 24 hours at 25 °C. Afterwards, the precipitate was filtered off and THF was removed under reduced pressure to obtain a yellow oil. The crude product was washed twice with dichloromethane (DCM) and saturated Na₂CO₃. DCM was removed under reduced pressure, then the crude product was dried using NaSO₄ and purified using column chromatography with DCM solvent to obtain a pale-yellow oil (95% yield).

Step 2 (hydrosilylation): Karstedt's catalyst (6 μL , 11 μmol) and dimethylethoxysilane (8.9 g, 85.4 mmol) were added to the product from step 1 (1.28 g, 4 mmol). The mixture was stirred overnight at room temperature under a nitrogen atmosphere. After removing the excess dimethylethoxysilane under reduced pressure, EDMP was stored at 20 °C. The synthesized ATRP initiator (EDMP) was characterized by ^1H NMR (Figure S1). The sample was prepared in a CDCl_3 solution and the measurement was acquired at 500 MHz. Peaks appear at $\delta =$ 0.21 (Si- CH_3); 0.61 (- CH_2 - CH_2 -Si-); 1.21(- CH_2 - CH_3); 1.23-1.60 (polymer backbone, - CH_2 -); 2.02 (- $\text{C}(\text{CH}_3)_2\text{Br}$); 3.83, 4.13 (-O- CH_2 - CH_2 -) ppm. The peaks at 3.5 ppm (- CH_2 -, 13) and \sim 0.1 ppm (Si- CH_3 , 12) result from some hydrolysis of the ethoxysilyl group of EDMP.

6.3.3. Pre-treatment of Ludox-TM40 particles

In the first step of the purification procedure, each of Dowex 50W X8 and Dowex 1X8 (both 50 g) were transferred to separate 600 mL beakers. The resins were washed with 3N NaOH, hot water, methanol, and cold water. After each individual wash, the resins were collected by filtration. This washing cycle was repeated 5 times for both resins. After the last wash cycle of Dowex 50W X8, the resin was converted to the hydrogen form by a final washing step using an excess amount of a 3N HCl solution. Likewise, Dowex 1X8 was converted to the hydroxy form with a 3N NaOH solution, whereas this step was performed shortly before use.

In the second step of purification, the Ludox TM-40 dispersion (100 mL) was diluted with 100 mL of MilliQ water, stirred, and added to Dowex 50W X8 resin in a beaker and agitated overnight. Ludox TM-40 particles were then collected via filtration and added to Dowex 1X8 resin in a beaker and stirred overnight. The particles were then collected via filtration, with large aggregates centrifuged down at 3000 rpm, then dialyzed against ethanol for 1 week.

6.3.4. Preparation of EDMP-functionalized Ludox TM-40 nanoparticles

The pre-treated Ludox particles were dispersed in ethanol (1 g, 50 mL) and added to a 200 mL round-bottom flask. Afterward, a pH of 10 was obtained by the addition of 28% NH_3 solution. EDMP (0.860 g, 0.002 mol) was then slowly added to the dispersion and refluxed for 24 hours at 85 °C. Finally, the particles were purified by dialysis against ethanol for one week, freeze-dried, and stored at 4 °C with minimized humidity. The amount of grafted EDMP was determined by TGA, see (Supporting Information, Figure S4).

6.3.5. Synthesis of silica-poly(methyl methacrylate) hairy nanoparticles

SiO_2 -EDMP nanoparticles (200 mg) were mixed with 10 mL of a Pluronic F-127 (0.04 g/mL) solution in a 20 mL scintillation vial and vortexed and sonicated until a milky white suspension was formed. In parallel, TBAB (1.934g, 6 mmol), CuBr_2 (1 mg, 4.48 μmol), Tris(2-pyridylmethyl) amine (TPMA) (12.2 mg, 42 μmol), and water (43.2 mL) were added in a 50 mL round-bottom Sample flask with a stirring bar. The particle suspension was added to the 100 mL Sample flask and degassed for 20 minutes by bubbling with argon. MMA (7.5-14.1 mmol/h) and an aqueous solution of ascorbic acid (2.27 mM, 3.6 mL, 1.4 $\mu\text{mol/h}$) were added to the Sample flask simultaneously over the course of 6 hours using two syringe pumps, (see Supporting Information, Scheme S2). In cases where the syringe pump was not precise enough to add the exact amount of MMA desired during the Sample, the pumping rate was adjusted so that all monomer would be added a short time before the Sample was terminated. After 6 hours, at which point the addition of both MMA and ascorbic acid was complete, the polymerization was terminated by opening the Sample to air. The hairy nanoparticles were separated by centrifuging at 4400 rpm for 20 minutes, washed twice with THF and MilliQ water, and dried in a vacuum oven at 80 °C; see Scheme 1b.

6.3.6. Instruments

Fourier-transform infrared spectroscopy (FT-IR) measurements were performed on a Vertex V80V vacuum FT-IR instrument; Bruker, Billerica, MA, USA. Samples analyzed with FT-IR were first ground into a fine powder. Spectra were acquired at 2 cm^{-1} resolution in the range of 4000 to 400 cm^{-1} with an integrating time of 1 min for each sample.

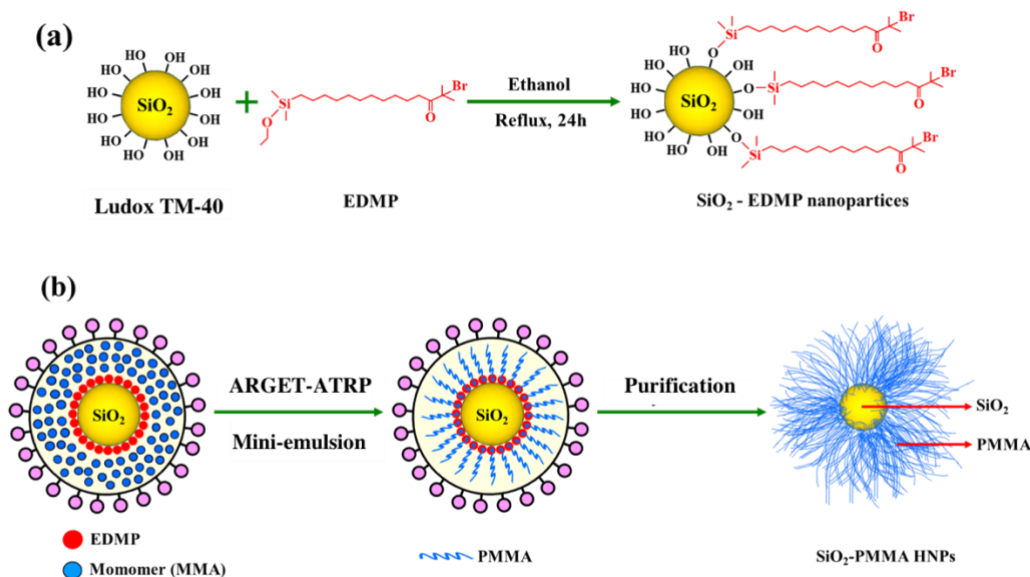
Thermogravimetric analysis (TGA) measurements were performed on a TA Instruments Inc. TGA Q500, heating the samples from 20°C to 600°C with a heating rate of $10^{\circ}\text{C}/\text{min}$ under a nitrogen atmosphere. The mass of the samples for each measurement was in the range of 8–10 mg.

The molar mass and polydispersity (\bar{M}_w/\bar{M}_n) of the grafted polymer chains were obtained after HF etching by using a Waters ambient temperature THF-GPC. A Waters 410 differential refractive index detector and a Waters 486 106 UV/Vis detector were applied in parallel. The three GPC columns used are PSS (Polymer Standards Service) SDV models with 8 mm x 300 mm dimensions, with porosities of 50 angstroms, 500 angstroms, and Linear M. Elugrams were obtained at 35°C using a THF flow rate of 1 mL/min and were calibrated with narrow polystyrene standards. The molar mass and the polydispersity \bar{M}_w/\bar{M}_n were analyzed using Breeze software. ^1H Nuclear Magnetic Resonance (NMR) spectra were measured using a Varian INOVA-500 NMR Spectrometer in CDCl_3 at 20°C with a $^1\text{H}/\text{BB}$ nanoprobe, and the data was recorded using VNMR 6.1C software. X-ray diffraction (XRD) measurements of the HNPs were carried out on Bruker-D8 Advance ECO powder diffractometer. Diffraction was measured using Cu K- α radiation with a wavelength of approximately $\lambda = 1.54\text{ \AA}$ and photon energy of $E = 8.04\text{ keV}$. The source of the 40 kV x 25 mA X-rays was a water-cooled fixed Cu target excited by an electron gun. Transmission electron microscope (TEM) images were collected by FEI F20 TEM STEM with a Thermo-Fisher GF20 scope, monochromated and

operated at 200 kV. The images were acquired in High Angular Annular Darkfield (HAADF) mode TEM.

6.4. Results and Discussion

The synthesis of HNPs was carried out in two steps. In the first step, Ludox TM-40 particles with a diameter of 25 nm were functionalized with the hydrophobic ATRP initiator, EDMP, as shown in Scheme 1(a). Subsequently, SiO₂-PMMA HNPs were synthesized via mini-emulsion ARGET-ATRP on the silica particle surfaces by adding MMA and ascorbic acid to a Pluronic F-127 surfactant-stabilized micellar emulsion over a period of 6 hours (Scheme 1(b)). TBAB acted as a shuttle to transport MMA through the aqueous phase to the surfactant-covered silica nanoparticle surfaces. With this method, the graft density, molar mass of grafted chains, and the corona diameter were tuned by changing the MMA feeding rate and the total MMA content; see Table 1, Samples 1-4.



Scheme 1. (a) Preparation of EDMP-functionalized SiO₂-nanoparticles. (b) Synthesis of SiO₂-PMMA HNPs using mini-emulsion ARGET-ATRP.

Table 1. SiO₂-PMMA HNPs synthesized using mini-emulsion ARGET-ATRP.

Sample	[MMA] (mol/L)	MMA Feeding Rate (mmol/h)	Polymer Content (wt%)	Graft Density ($\mu\text{mol}/\text{m}^2$)	M_n	Canopy Thickness (nm) ^a
1	0.67	7.5	21	0.018	86400	2.5 \pm 0.3
2	1.00	10.3	25	0.019	106200	7.0 \pm 1.0
3	1.17	12.2	32	0.028	105800	11.0 \pm 1.6
4	1.34	14.1	61	0.039	276300	-
5 ^b	0.67	-	32	0.014	214300	-
6 ^{b,c}	0.67	-	50	0.021	328700	-
7 ^{b,c,d}	0.67	-	53	0.048	158600	-

^a The diameters of SiO₂-PMMA HNPs were determined by averaging the diameters of 10 particles measured by TEM and analyzed with ImageJ. ^b All MMA was added at the beginning of the Sample. ^c With acetone (20 vol%). ^d Without TBAB.

Following synthesis, the SiO₂-PMMA HNP samples were characterized by FT-IR and XRD measurements (Supporting Information, Figure S2, S3). The FT-IR spectra of the sample described in Table 1, Sample 5 shows bands at $\nu = 1730 \text{ cm}^{-1}$ (w, -C=O) and $2997\text{-}2952 \text{ cm}^{-1}$ (w, -CH₂-CH₃-), characteristic of PMMA, as well as a band at $\nu = 1100 \text{ cm}^{-1}$ (s, -Si-O-Si-) from the silica nanoparticles, indicating a successful polymerization of PMMA on the particle surface. In addition, X-ray diffraction measurements ($2\theta = 10\text{-}70^\circ$) confirmed the existence of PMMA on the silica nanoparticles, due to the observed peak at $2\theta = 22.4^\circ$ from SiO₂ nanoparticles and a PMMA peak at $2\theta = 24.5^\circ$, see Figure S3. The graft density and the molar mass of the grafted PMMA chains were determined (Supporting Information, Equation S1) by performing TGA measurements (Figure 1(a)) of the HNP samples, in addition to GPC measurements after HF etching of the SiO₂ cores.

A series of 6-hour experiments was performed by varying the MMA feeding rate, leading to total added MMA concentrations ranging from $c = 0.67$ mol/L to $c = 1.34$ mol/L (Table 1, Samples 1-4). Increasing the amount of MMA added over a period of 6 hours led to an increase in the graft density and molar mass of the grafted PMMA chains, as seen in Figure 1(b).

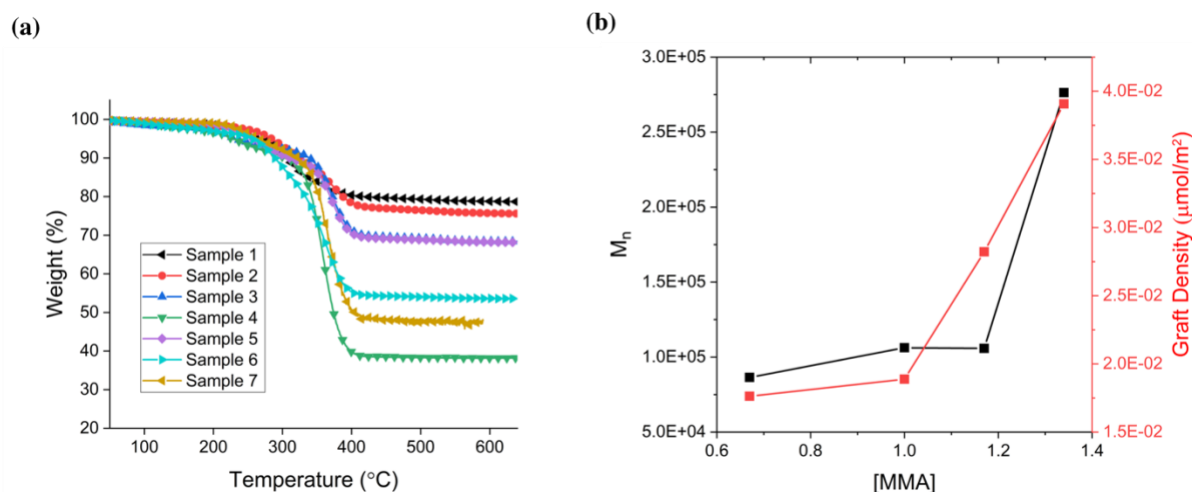


Figure 1. (a) TGA measurements of the HNP samples described in Table 1, Samples 1-7. The polymer content (wt%) was calculated from the weight change between 30°C and 600°C. (b) The dependence of PMMA graft density and molar mass on the monomer concentration (Table 1, Samples 1-4).

With an MMA concentration of $c = 0.67$ ml/L, a polymer content of 21 wt% and a molar mass of $M_n = 86400$ were obtained, from which a graft density of $0.018 \mu\text{mol}/\text{m}^2$ was calculated (Table 1, Sample 1). For the increased monomer concentration of $c = 1.00$ mol/L, a polymer content of 25 wt%, molar mass of $M_n = 106200$, and graft density of $0.019 \mu\text{mol}/\text{m}^2$ were achieved. Finally, when the monomer concentration reached its highest value at $c = 1.34$ mol/L, the polymer content increased to 61 wt% with a molar mass of $M_n = 276300$ and a graft density of $0.039 \mu\text{mol}/\text{m}^2$ (Table 1, Samples 2-4).

The samples from Samples 1 and 5 in Table 1 shared the same final concentration of added MMA. While monomer was added continuously for Sample 1, all MMA was present at the beginning of the Sample 5 Sample. As a result, the Sample 5 HNPs possessed higher polymer

content and molar mass than those of Sample 1. However, the final Sample mixture in Sample 5 contained ungrafted PMMA at an undesirable 20 wt% of the total added monomer, compared to the preferred 0 wt% measured for Sample 1, as measured by precipitating ungrafted polymer in methanol. The presence of high amounts of ungrafted polymer may lead to Sample delocalization and subsequent aggregation, as discussed later. One possible explanation is that ungrafted PMMA forms when polymer chains and initiators are cleaved from the particle surfaces. If an ungrafted polymer chain or initiator is surrounded by excess monomer, it may undergo polymerization separate from the particle surface. Controlled monomer feeding, as in Sample 1, may limit this phenomenon. Table S1 in the Supporting Information contains data for the amount of ungrafted PMMA measured for each of the Samples.

Ugelstad *et al.*¹³ developed seeded emulsion polymerizations using water-soluble solvents including acetone. The use of two solvents increased the entropy of particle mixtures, which in turn facilitated the swelling of micelles with monomer. Motivated by Ugelstad *et al.*'s work, Cordero *et al.*¹⁴ introduced acetone in mini-emulsion ARGET-ATRP of PMMA to both increase the solubility of monomer in the aqueous phase and assist in the diffusion of monomer to the micellar oil phase, thereby localizing polymerization in the micelles. Cordero *et al.* additionally used TBAB as a phase transfer agent to help to shuttle monomer into the micelles, due to the finite solubility of TBAB in both phases.

In the present work, the roles of TBAB and acetone, both presumed to support the transport of monomer into the micelles, were investigated with a constant MMA concentration of $c = 0.67$ mol/L (Table 1, Samples 5-7). For these experiments, all monomer was added to the Sample flask immediately, rather than using a syringe pump, to replicate the conditions of earlier experiments.¹⁴ The Sample in Sample 5 was conducted with TBAB and without acetone, similar to Samples 1-4. To understand the impact of acetone, Sample 6 was conducted with both TBAB and acetone. The HNPs described in Sample 6 show higher polymer content (50

wt%), higher graft density ($0.021 \mu\text{mol}/\text{m}^2$), and higher molar mass ($M_n = 328700$) than those in Sample 5. However, the amount of ungrafted PMMA created in this Sample was 40 wt% of the total monomer, about twice the 20 wt% ungrafted PMMA seen in Sample 5. A possible explanation of this observation could be that acetone not only assisted in the diffusion of MMA into the micelles but also increased the transfer of MMA and short polymer chains out of the micelles, leading to the detection of ungrafted PMMA. The experiment in Table 1, Sample 7 was performed with acetone but without TBAB. The HNPs in Sample 7 show a polymer content of 53 wt%, as well as an ungrafted PMMA content of 36 wt% of the total monomer. These results are similar to those of Sample 6, which included both acetone and TBAB, though the molar mass $M_n = 158600$ is half that of Sample 6, and graft density $0.048 \mu\text{mol}/\text{m}^2$ is twice that of Sample 6. A possible explanation for this discrepancy is that the TBAB-assisted transfer of monomer into micelles results in the increase of initial MMA concentration. In turn, this would lead to a higher initial number of growing chains on the surface and thus a higher graft density.

The diameters and the core/corona ratios of the SiO_2 -PMMA HNPs were determined by darkfield TEM measurements. The TEM images of the SiO_2 -PMMA HNPs described in Table 1, Samples 1-4 are shown in Figure 2. As shown in Figure 2, the SiO_2 -PMMA HNPs exhibit a spherical core-shell morphology with varying PMMA corona thickness. The ungrafted Ludox TM-40 cores were measured by TEM to have an average diameter of 25 nm. The corona thickness of each sample was calculated by subtracting the ungrafted core radius from the average radius of the HNPs, as measured by TEM. As might be expected, increasing MMA concentrations led to larger PMMA coronas until the onset of aggregation at an MMA concentration of $c = 1.34 \text{ mol}/\text{L}$. For the samples described in Table 1, Samples 1-3, we calculated corona thicknesses of $2.5 \pm 0.3 \text{ nm}$, $7.5 \pm 1.0 \text{ nm}$, and $11.0 \pm 1.6 \text{ nm}$ (Figure 2(a-c; e-g)), respectively. As seen in Figure 2(d, h), TEM images of the Sample 4 sample showed

large aggregates of particles embedded in PMMA reaching sizes of 200-300 nm, and thus the corona thickness could not be calculated. The aggregation in Sample 4 might be explained by the presence of ungrafted PMMA at 16 wt% of the total added monomer, while no ungrafted polymer was observed for Samples 1-3. These observations demonstrate that the corona thickness can be tuned by varying the MMA concentration, although, for high enough MMA concentrations, excess ungrafted polymer can lead to HNP aggregation.

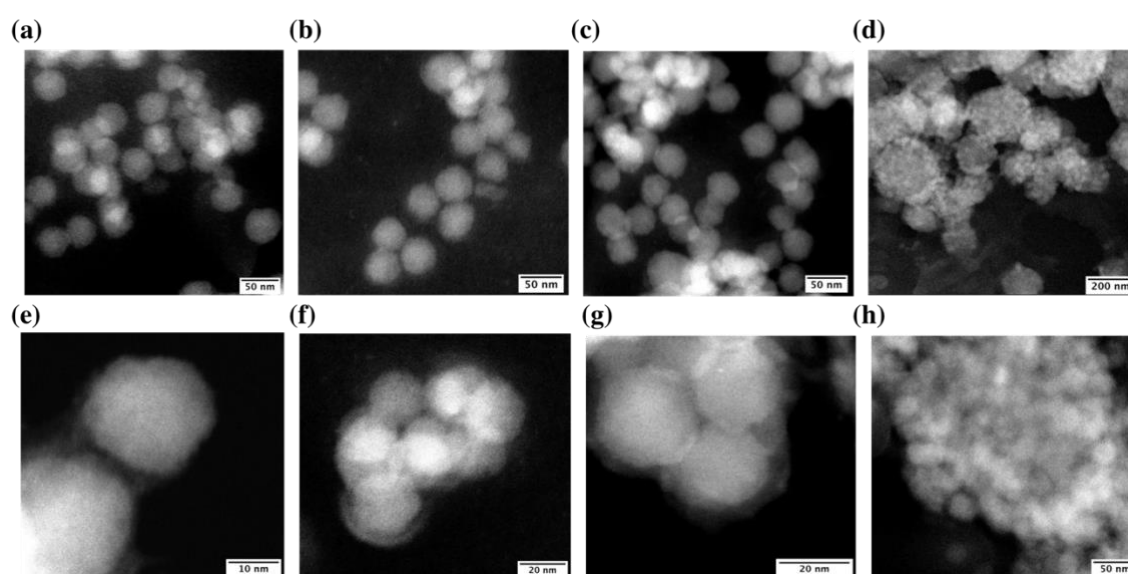


Figure 2. TEM images of the SiO₂-PMMA HNPs obtained via mini-emulsion ARGET-ATRP with varying polymer content (Table 1, Samples 1-4). (a, e). Sample 1, (b, f). Sample 2, (c, g). Sample 3, (d, h). Sample 4.

In order to qualitatively understand the time-dependence of the polymer grafting process, a study of Sample kinetics was performed by regularly extracting samples from a Sample using the same conditions described for Table 1, Sample 1. The results of this experiment are shown in Figure 3. The molar mass and polymer weight content of the HNPs increase for approximately 2 hours, then become constant at approximate values of $M_n = 78000$ and 21 wt%, respectively. As a result, the polymer graft density calculated according to Pasetto *et al.*¹⁵ reaches a value of $0.021 \mu\text{mol}/\text{m}^2$ at 2 hours, and remains constant around $0.02 \mu\text{mol}/\text{m}^2$ for the remainder of the Sample. It follows that future SiO₂-PMMA HNP synthesis times may be

reduced to around 2 hours, instead of 6 hours, without significantly impacting the final graft density.

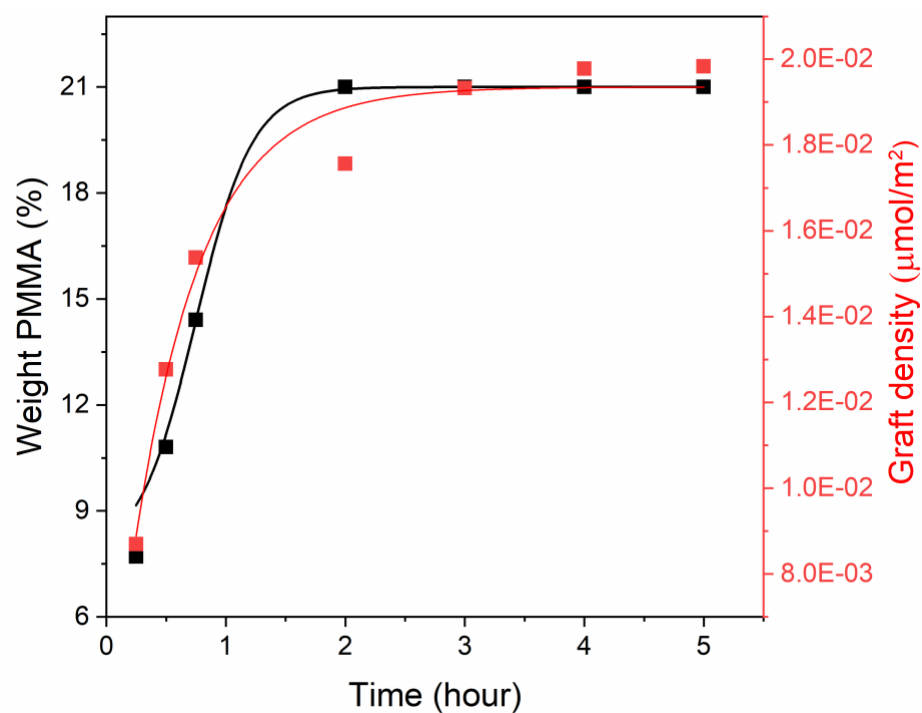


Figure 3. Polymerization kinetics for the grafting of PMMA from silica nanoparticles in mini-emulsion ARGET-ATRP. $[\text{MMA}] = 0.67 \text{ mol/L}$; MAA feeding rate = 7.5 mmol/h at $80 \text{ }^\circ\text{C}$. The curves are drawn as a guide to the eye.

6.5. Conclusion

PMMA-SiO₂ HNPs were prepared using ARGET-ATRP in mini-emulsion. Silica nanoparticles with a diameter of 25 nm were initially functionalized with hydrophobic ATRP initiators (EDMP), then PMMA was polymerized on the particle surfaces. TBAB and acetone were both presumed to aid the transport of monomer into the micelles to localize the polymerization of PMMA on the particle surfaces. Acetone led to the formation of ungrafted PMMA, while the use of TBAB alone was sufficient for monomer transport. Qualitative Sample kinetics show that the graft density remained constant at 0.02 $\mu\text{mol}/\text{m}^2$ after 2 hours. By changing the MMA feeding rate, the graft densities varied from 0.018 $\mu\text{mol}/\text{m}^2$ to 0.039 $\mu\text{mol}/\text{m}^2$ with corona thicknesses of 2.5 nm to 11 nm, respectively. This method enables a straightforward, aqueous synthesis of HNPs, which has great potential for future large-scale production.

6.6. Acknowledgments

This work was performed in part at the Cornell NanoScale Facility, a member of the National Nanotechnology Coordinated Infrastructure (NNCI), which is supported by the Air Force Office of Scientific Research (AFOSR FA9550-17-1-0038) , and for prior support, the Air Force Research Laboratory (AFRL). This work made use of the Cornell Center for Materials Research Shared Facilities which are supported through the NSF MRSEC program (DMR-1719875). We are grateful for the scientific and technical assistance from Cornell's Center for Nanomaterials Engineering and Technology.

6.7. Supporting Information

The grafting density G_P is calculated according to Pasetto *et al.*¹⁵ using

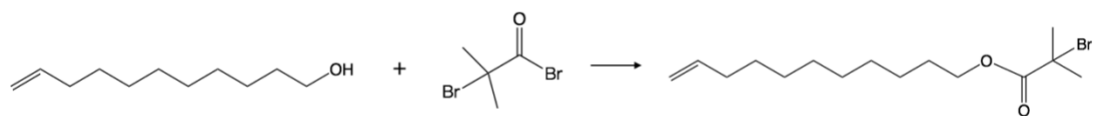
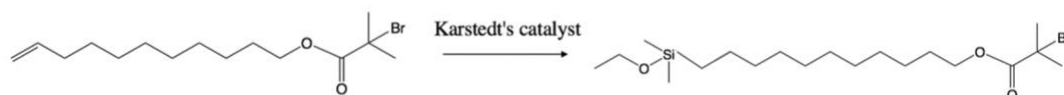
$$G_P = \frac{\frac{W\%_{\text{polymer+initiator}}}{100-W\%_{\text{polymer+initiator}}} - \frac{W\%_{\text{initiator}}}{100-W\%_{\text{initiator}}}}{M_n \cdot S_{sp}} \cdot 10^6 \left(\frac{\mu\text{mol}}{\text{m}^2} \right),$$

where $W\%_{\text{initiator}}$ is the % weight loss of the initiator-functionalized silica cores prior to polymerization during TGA between 30°C and 600°C, $W\%_{\text{polymer+initiator}}$ is the % weight loss of the HNPs during TGA between 30°C and 600°C, M_n is the molar weight of grafted polymer chains in g/mol, and S_{sp} is the specific surface area of the Ludox TM-40 nanoparticles in m²/g. According to Sigma Aldrich, S_{sp} for the nanoparticles used is approximately 140 m²/g.

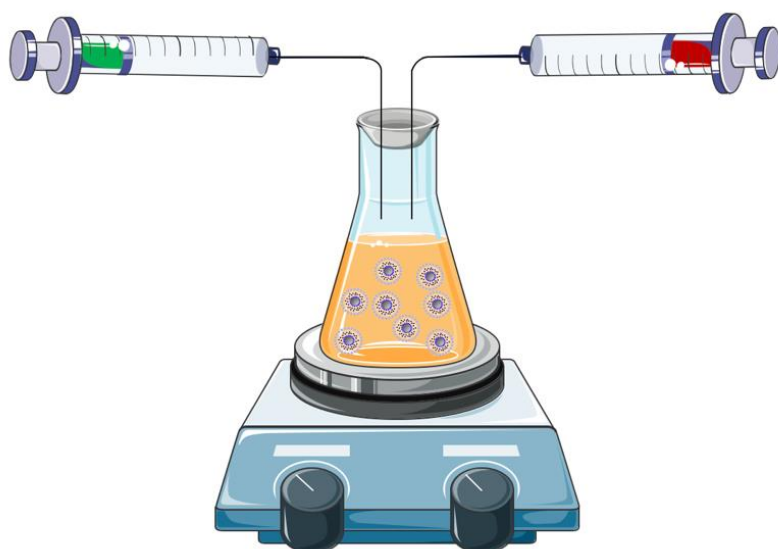
Table S1. Ungrafted PMMA for different Sample conditions in mini-emulsion ARGET-ATRP, calculated as weight % of the total mass of monomer added.

Sample	[MMA] (mol/L)	MMA Feeding Rate (mmol/h)	Ungrafted PMMA (wt%)
1	0.67	7.5	0
2	1.00	10.3	0
3	1.17	12.2	0
4	1.34	14.1	16
5 ^a	0.67	-	20
6 ^{a, b}	0.67	-	40
7 ^{a, b, c}	0.67	-	36

^a All MMA was added at the beginning of the Sample. ^b With acetone (20 vol%). ^c Without TBAB.

Step 1 (Bromination)**Step 2 (Hydrosilylation)**

Scheme S1. Two-step synthesis of 11-(ethoxydimethylsilyl) undecyl 2-bromo-2-methylpropanoate (EDMP) ATRP initiator.



Scheme S2. Synthesis of SiO₂-PMMA HNPs using mini-emulsion ARGET-ATRP. MMA was added with feeding rates that varied from 7.5 mmol/h to 14.1 mmol/h, and ascorbic acid was added at a constant rate of 1.4 μ mol/h. Prior to this step, Ludox TM-40 silica particles (d=25nm) were functionalized with the hydrophobic ATRP initiator, EDMP.

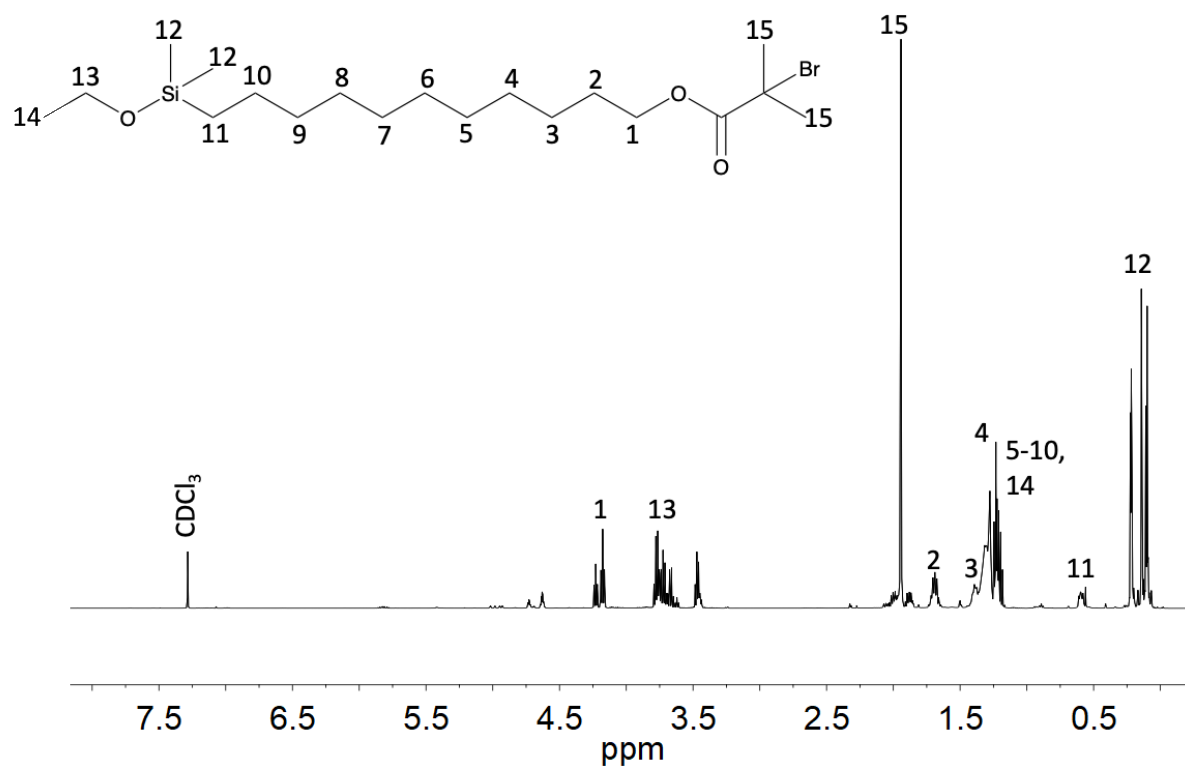


Figure S1. The NMR spectrum of EDMP, the ATRP initiator. The sample was prepared in a CDCl₃ solution and the measurement was acquired at 500 MHz. Peaks appear at δ = 0.21 (Si-CH₃); 0.61 (-CH₂-CH₂-Si-); 1.21(-CH₂-CH₃); 1.23-1.60 (polymer backbone, -CH₂-); 2.02 (-C(CH₃)₂Br); 3.83, 4.13 (-O-CH₂-CH₂-) ppm. The peaks at 3.5 ppm (-CH₂-, 13) and ~ 0.1 ppm (Si-CH₃, 12) result from some hydrolysis of the ethoxysilyl group of EDMP.

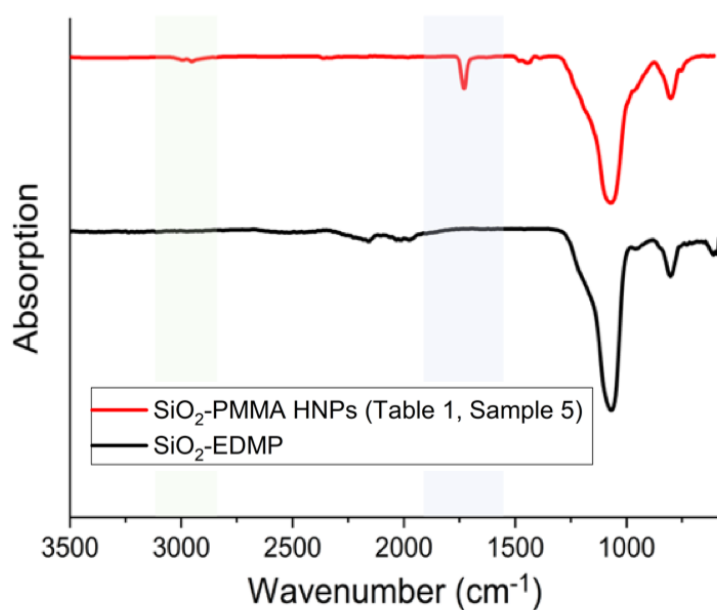


Figure S2. FT-IR spectra of the nanoparticles. HNPs described in Table 1, Sample 5: $\nu=1730$ (*w*, -C=O, PMMA), $\nu=2997-2952$ (*w*, -CH₂-CH₃-, PMMA), and $\nu=1100$ cm⁻¹ (*s*, -Si-O-Si-). SiO₂-EDMP nanoparticles: $\nu=1100$ cm⁻¹ (*s*, -Si-O-Si-) cm⁻¹.

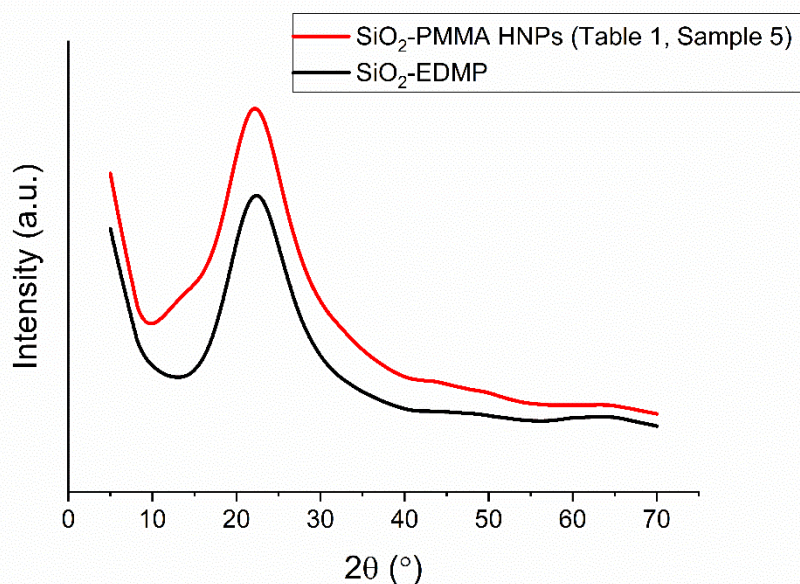


Figure S3. XRD of the initiator-functionalized silica cores, as well as the HNPs described in Table 1, Sample 5. SiO₂-EDMP HNPs: $2\theta = 22.4^\circ$ (*s*, SiO₂); $2\theta = 43.2^\circ$ (*w*, PMMA). Ungrafted SiO₂-EDMP nanoparticles: $2\theta = 22.4^\circ$ (*s*, SiO₂).

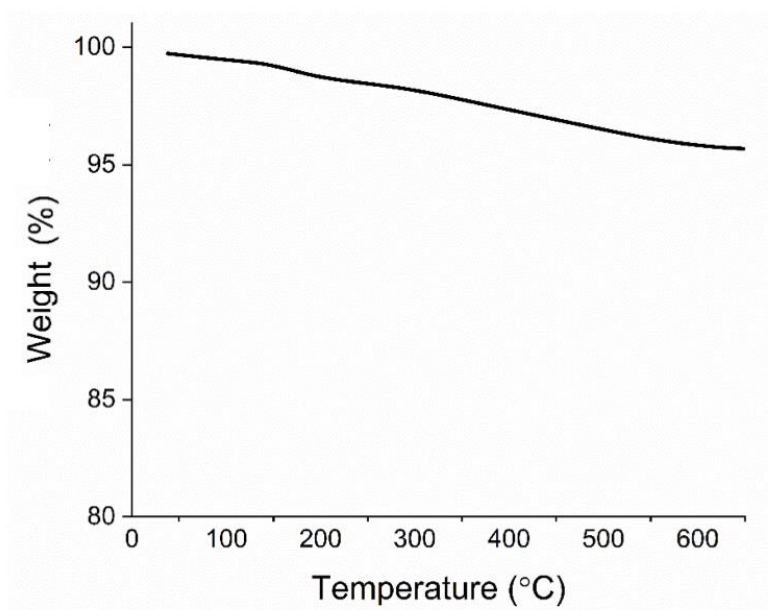


Figure S4. TGA measurement of the ungrafted SiO₂-EDMP nanoparticles. The initiator content $W\%_{\text{initiator}}$ (wt%) was calculated from the weight change between 30°C and 600°C.

6.8. References

- (1) Fernandes, N. J.; Koerner, H.; Giannelis, E. P.; Vaia, R. A. Hairy nanoparticle assemblies as one-component functional polymer nanocomposites: opportunities and challenges. *MRS Commun.* 2013, 3 (01), 13-29.
- (2) Kumar, S. K.; Jouault, N.; Benicewicz, B.; Neely, T. Nanocomposites with polymer grafted nanoparticles. *Macromolecules* 2013, 46 (9), 3199-3214.
- (3) Akcora, P.; Liu, H.; Kumar, S. K.; Moll, J.; Li, Y.; Benicewicz, B. C.; Schadler, L. S.; Acehan, D.; Panagiotopoulos, A. Z.; Pryamitsyn, V.; Ganesan, V.; Ilavsky, J.; Thiagarajan, P.; Colby, R. H.; Douglas, J. F. Anisotropic self-assembly of spherical polymer-grafted nanoparticles. *Nat. Mater.* 2009, 8 (4), 354-9.
- (4) Jayaraman, A. Polymer grafted nanoparticles: Effect of chemical and physical heterogeneity in polymer grafts on particle assembly and dispersion. *J. Polym. Sci. Part B: Polym. Phys.* 2013, 51 (7), 524-534.
- (5) Wang, J.-S.; Matyjaszewski, K. Controlled/"living" radical polymerization. atom transfer radical polymerization in the presence of transition-metal complexes. *J. Am. Chem. Soc.* 1995, 117 (20), 5614-5615.
- (6) Pyun, J.; Jia, S.; Kowalewski, T.; Patterson, G. D.; Matyjaszewski, K. Synthesis and Characterization of Organic/Inorganic Hybrid Nanoparticles: Kinetics of Surface- Initiated Atom Transfer Radical Polymerization and Morphology of Hybrid Nanoparticle *Ultrathin Films.* *Macromolecules* 2003, 36 (14), 5094–5104.
- (7) Min, K.; Gao, H.; Matyjaszewski, K. Preparation of homopolymers and block copolymers in miniemulsion by ATRP using activators generated by electron transfer (AGET), *J. Am. Chem. Soc.* 127 (11) (2005) 3825–3830.
- (8) Matyjaszewski, K.; Tsarevsky, N. V. Macromolecular engineering by atom transfer radical polymerization. *J. Am. Chem. Soc.* 2014, 136 (18), 6513-6533.

- (9) Landfester, K. Miniemulsion polymerization and the structure of polymer and hybrid nanoparticles. *Angew. Chem. Int. Ed. Engl.* 2009, 48 (25), 4488-4507.
- (10) Bombalski, L.; Min, K.; Dong, H.; Tang, C.; Matyjaszewski, K. Preparation of well-defined hybrid materials by ATRP in miniemulsion. *Macromolecules* 40 (21) (2007) 7429–7432.
- (11) Min, K. Gao, H.; Yoon, J-A.; Wu, W.; Kowalewski, T.; Matyjaszewski, K. One-Pot Synthesis of Hairy Nanoparticles by Emulsion ATRP. *Macromolecules* 42, 5, (2009) 1597-1603.
- (12) Goel, V.; Pietrasik, J.; Poling-Skutvik, R.; Jackson, A.; Matyjaszewski, K.; Krishnamoorti, R. Structure of block copolymer grafted silica nanoparticles. *Polymer* 2018, 159, 138-145.
- (13) Ugelstad, J.; Kaggerud, K. H.; Hansen, F. K.; Berge, A. Absorption of Low Molecular Weight Compounds in Aqueous Dispersions of Polymer-Oligomer Particles, 2. A Two Step Swelling Process of Polymer Particles Giving an Enormous Increase in Absorption Capacity. *Macromol. Chem. Phys.* 1979, 180 (3), 737–744.
- (14) Cordero, R.; Jawaid, A.; Hsiao, M.S.; Lequeux, Z.; Vaia, R. A.; Ober C.K. Mini Monomer Encapsulated Emulsion Polymerization of PMMA Using Aqueous ARGET ATRP. *ACS Macro Lett.* 2018, 7, 4, 459-463.
- (15) Pasetto, P.; Blas, H.; Audouin, F.; Boissiere, C.; Sanchez, C.; Save, M.; Charleux, B. Mechanistic Insight into Surface-Initiated Polymerization of Methyl Methacrylate and Styrene via ATRP from Ordered Mesoporous Silica Particles. *Macromolecules* 2009, 42, 5983–5995.

7. CHAPTER 2. THREE DIMENSIONAL PRINTING OF ZINC-OXIDE NANOSTRUCTURES FOR MULTIFUNCTIONAL APPLICATIONS

7.1. Abstract

Three-dimensional (3D) printing has gained increasing interest and is now being applied to broader fields; however, the materials of choice are still mostly limited to polymers. Herein, we report the first 3D-printable Zn oxide nanoparticles (NPs) for digital light processed 3D printing that enable the fabrication of arbitrary and complex 3D metal oxide patterns. By modifying photosensitive methacrylic acid on ZnO NPs (ZnO-MAA NPs), we demonstrate the production of programmable 3D structures purely from nanoscale building blocks. 3D printed techniques enable processing ZnO 3D structure at room temperature and the XRD result shows the structure of 3D printed ZnO NPs is amorphous. We show printing of structures with a resolution approaching 50 μm , which is four times higher than current techniques with a height variation of only several nanometers. We go on to demonstrate electronic properties of this material and show that this process can be applied to 3D printed electronically conductive pathways, thereby opening up opportunities for a broad range of 3D printed metal mesostructures in applications to optoelectronics.

Keywords: 3D optical printing; inorganic-organic hybrid nanoparticles; ligand stripping; electronic properties,

7.2. Introduction

Additive manufacturing (i.e., 3D printing) has evolved along an impressive trajectory over the last few years.^{1,2} Whereas 3D printers were initially applied for rapid prototyping (mostly from plastics), recent advances have demonstrated the ability to fabricate more complex materials and devices including biological tissues,³ batteries,⁴ and optoelectronic devices.^{5,6} Despite this rapid progress, bringing the heralded prospects of 3D printing to full technological fruition requires advances in the range of material compositions that can be printed. Metal oxides provide a particularly interesting material class for 3D printing by virtue of their diverse range of applications spanning biomedical, catalytic and optoelectronic devices.^{7, 8}

Zinc oxide is a widely studied metal oxide, and is widely used in the semiconductor industry due to its photocatalytic and piezoelectric efficiency.^{9,10} It has a band gap of ca. 3.36 eV, an excitation energy of 60 meV, and high photosensitivity under extreme ultraviolet light.¹¹ Additionally, it is inexpensive,¹² has anti-ultraviolet (UV) properties,¹³ and environmental friendliness.^{14,15} Nevertheless, metal oxides are not easily machined or cast. Defects created during fabrication lead to brittleness, low ductility and cracking¹⁶ Additionally, metal oxides have very high melting points, which increases the difficulty of processing them by additive manufacturing, especially for complicated structures.¹⁷

Prior efforts to 3D print ZnO have focused on extrusion methods. Tubío et al.¹⁸ explored using ZnO in 3D printing inks. The ink was formed by dispersing ca. 0.7- μm ZnO particles in deionized water and combining them with poly(acrylic acid). ZnO-ABS composite filaments for 3D printing were also reported.¹⁹ However, low resolution, low printing speed and high roughness remain as issues that must be overcome. For example, the extrusion-based additive manufacturing method currently limits the resolution to about several hundred micrometers.

In this report, we demonstrate 3D-printable ZnO building blocks having photoresponsive ligands, specifically methacrylic acid (MAA), on the surface of NPs. Programmable 3D

structures were precisely constructed from the nano- to macro-scale based on the building units. MAA ligands play a critical role in increasing colloidal stability. Exposed photo-radical generator stripped off methacrylic acid ligands and result in a solubility change, to form the pattern. Optical and scanning electron microscopy (SEM) images revealed that the printed sample has good resolution (ca. 50 μm). Also, 3D printed ZnO films show lower resistivity and rectifying behavior after calcined. This study suggests the possibility of using metal-oxide customized 3D structures made from NP building blocks in future semiconducting device.

7.3. Methods

5.3.1 Materials

The ZnO (99%), MAA (99%), C-ZnO NPs dispersion (< 110-nm particle size; 40 wt% in butyl acetate), ethylene glycol, ethyl acetate (EA) and dichloromethane (DCM) were purchased from Sigma–Aldrich (St. Louis, MO, USA). Silicon wafers were purchased from WRS Materials (San Jose, CA, USA). Diphenyl (2,4,6-trimethylbenzoyl) phosphine oxide (TPO; Sigma) was used as a photoradical generator. All buffers and other reagents were of the highest purity grade commercially available.

7.3.2. Synthesis and patterning of ZnO-MAA NPs

Figure S1 schematically illustrates the Sample of ZnO and MAA. ZnO and MAA were slowly added to ethyl acetate with stirring in the dark to produce a milky dispersion. ZnO-NPs were prepared using a method similar to that employed to synthesize HfO₂- and ZrO₂-based NPs.²⁰ The dispersion was allowed to continuously stir for 7 days; the color of the solution gradually changed from milky white to transparent light yellow as the ZnO-MAA NPs became uniformly distributed in the EA solvent. The EA solvent was then removed at 70mmHg; orange ZnO-MAA NPs remained.

Figure S2 demonstrates the hypothetical pathway by which the ZnO ink can react in response to photoexposure. The mechanism is the ligand stripping at the surface of NPs with photoactive compound for photolithography technique.²¹⁻²⁴ Photo-radical generated by UV exposure will strip off the methacrylic acid ligands and lead to a solubility change, which forms the pattern.

7.3.3. Fabrication of 3D printed amorphous ZnO film

The build-stage for the printed structure was provided by a silicon wafer placed in the bottom of the 3D printing reservoir. We prepared a DCM suspension of ZnO-MAA NPs before 3D fabrication. TPO was used as a photoradical generator for the Sample. The vial was flushed with a flow of N₂ for 10 mins to remove oxygen. The solution was then loaded into a syringe, transferred to the 3D printing reservoir and used to print films of dimensions 2 cm × 2 cm × 100 μm on a silicon wafer that cured into amorphous ZnO films upon exposure to UV light (3 mW/m² for 385-nm wavelength) for 50 s. The silicon wafer was removed from the 3D printing reservoir and washed with 30 mL of DCM for 3 s. Repetition of these steps produced 3D objects.

7.3.4. Preparation of TEM samples

A ZnO film specimen was trimmed onto a Cu-coated transmission electron microscopy (TEM) grid using a focused ion beam (FIB). Samples were imaged at an accelerating voltage of 200 kV. Atomically resolved high-resolution TEM images were used to characterize the surface morphologies.

7.3.5. Instruments

A custom-built digital 3D processing machine equipped with a UV light (385 nm and 3 mW/cm²) was used to prepare ZnO films at 20°C. The optical properties of films were determined by UV-visible (UV-vis) spectroscopy using a Cary 5000 UV-vis near-infrared (NIR) spectrophotometer. Fourier transform-infrared (FT-IR) (Vertex V80V vacuum FT-IR; Bruker, Billerica, MA, USA) spectroscopy was used to confirm bonding to the ZnO-MAA NPs during the microemulsion Sample. Samples for FT-IR analysis were ground into fine powder using a mortar and pestle.

Dynamic light scattering (DLS) (Zetasizer Nano 90; Malvern, Worcestershire, UK) was used to measure the hydrodynamic diameter of NPs dispersed in the solvent. Three measurements were recorded for each sample. The atomic force microscopy (AFM) images were recorded on an Agilent 550 instrument (Agilent Technologies, Santa Clara, CA, USA) with silicon cantilevers and a spring constant of 20–30 N/m. The resonance frequencies ranged from 140 to 160 kHz and the scan speed varied from 0.5 to 1.0 line/s. The amorphous ZnO film was studied with a Tecnai F20 TEM (FEI, Hillsboro, OR, USA) coupled with energy dispersive spectroscopy (EDS) capability at 200 kV. A ZnO film sample for TEM examination was prepared using a Ga⁺ ion source FIB to mill the specimen. To minimize beam damage, a thin carbon film was deposited onto the sample surface before FIB milling. Different milling conditions were used for rough and final milling. Rough milling was carried out at an operating voltage of 30 kV and a beam current of 6.8 nA; final milling was conducted at an operating voltage of 5 kV and a lower beam current of 40 pA. Sample morphologies were observed using a field-emission scanning electron microscope (Mira3 FE-SEM; TESCAN USA Inc., Warrendale, PA, USA) at an accelerating voltage of 2 kV. Thermogravimetric analysis (TGA) was performed on a TGA Q500 instrument (TA Instruments Inc.) at a heating rate of 10°C/min to 700°C under a nitrogen atmosphere with a sample size of 8–10 mg.

7.3.6. Transmission line measurement

The experimental setup of transmission line measurement is shown in Figure S3(a). Electrical resistivity was measured by laminated copper contacts, a probe station and Source Measure Unit (SMU) Instruments (Keithley Series 2400). Copper contacts were deposited on silicon wafer by photolithography and electron beam evaporation in ZnO film. The distances between the copper contacts were 10, 20 and 30 μm in Figure S3(b). These deposited wafers were washed with acetone and ethanol. Then, ZnO films were printed on these wafers. Thermally

annealed samples were prepared by air furnace under 700°C (The calcination rate is 10°C/s). We used a probe station to apply a voltage between two copper contacts and measured the current flow. The values presented are the averages of five measurements.

7.4. Results and Discussion

7.4.1. Dispersion and characterization of ZnO-MAA NPs

Photoresponsive ZnO inks were formed by functionalizing the ZnO NP surface with MAA. The resulting ZnO-MAA ink can be readily dispersed in polar organic solvents like dichloromethane (DCM). ZnO-MAA NPs are highly soluble in DCM solvent. Photosensitive ZnO-MAA NPs, induced by a photoradical generator, form an insoluble ZnO-MAA NP film. The film consisted of small ZnO particle size enables the formation of smooth ZnO surfaces with height differences of only several nanometers. Figure 1(a) schematically illustrates the chemical structure of the ZnO-MAA NPs and the 3D printing process.

To understand how the NPs surface chemistry changes during photo-exposure and development we turned to FT-IR spectroscopy. The FT-IR spectra of the MAA and ZnO-MAA NPs are presented in Figure S4. The ZnO-MAA NPs displayed a peak at 1,640 cm^{-1} due to C=C bond stretching in the methacrylate group and peaks at 2,870- 2,950 cm^{-1} corresponding to C-H bond stretching.²⁵ Coordination bonding between Zn and the methacrylate group (COO-Zn) is evidenced by bands at 1,551 cm^{-1} (C=O), 1,412 cm^{-1} (C-O) and 491 cm^{-1} (Zn-O-C).²⁶ The peak at 1,720 cm^{-1} is related to free MAA.²⁷ The shoulders in the spectra represent the methacrylate groups in modified-ZnO. Changes in the peaks at 2,800–3,000 cm^{-1} in Figure S4 were attributed to changes in alkane C-H bonds caused by the methacrylate groups in the modified ZnO. After photoexposure, we found that the ZnO film peak at 1,640 cm^{-1} and 690-950 cm^{-1} C=C bond stretching slightly decreases, but 2,870- 2,950 cm^{-1} C-H bond stretching

peak increased. These changes are due to ligand stripping, which results in the solubility changes after UV exposure.

An ideal ZnO-MAA NPs ink requires good dispersibility, radical stability and light transparency in solvent; otherwise, NPs ink will create many defects during the process or become unprintable. We compare several aliphatic and aromatic solvents (Figure S5) and find DCM enables the formation of defect-free patterns (Figure S5(a)). We dispersed ZnO-MAA NPs in DCM. The solution was still transparent at a concentration of 20 wt%, which indicates good dispersibility in DCM. On the other hand, aromatic solvents such as toluene appear to diminish the reactivity of free radicals and create a milky sample with many defects (Figure S5(b)). Moreover, bad solubility will lead to an unprintable result. Figure S5(c) indicates that ZnO-MAA NPs cannot be dispersed in hexane, which become unprintable.

Surface modified ZnO NPs with MAA ligands improve the dispersibility in organic solvent. The particle sizes of the ZnO-MAA NPs, C-ZnO NPs and ZnO powder were measured using DLS (Figure 1b). The solution used for the measurements contained 200 mg of NPs and 10 mL of DCM. Although the C-ZnO NPs did not precipitate after 1 day, the color of the solution was milky. This was due to the large size of the C-ZnO NPs and aggregation with a particle size distribution of 30–110 nm. Also, the ZnO powder in DCM showed poor dispersion ability; after 1 day, most of the ZnO powder had precipitated (Figure 1c). As expected, ZnO powder has a large particle size distribution of 900–1,100 nm. On the other hand, the measurement results indicated ZnO-MAA NPs are monodispersed in DCM with a particle size of ca. 3–5 nm.

To study the optical properties of ZnO-MAA NPs in DCM, we measured the UV-vis spectrum. The UV-vis absorption spectrum of the C-ZnO NPs showed a broad absorption peak at ca. 371 nm (dotted line) and it is noteworthy that C-ZnO NPs exhibits high UV light absorption. After modification by MAA ligands, the UV-vis absorption spectrum of the ZnO-

MAA NPs in DCM solvent showed only an absorption peak at 258 nm (solid line) (Figure 2(a)). The absorption at 258 nm is attributed to the organic ligand (MAA). Figure 2(a) shows only an absorption peak at 258 nm for the ZnO-MAA NPs, which is not present in the spectrum of the C-ZnO NPs. Meanwhile, there is no absorption at wavelengths longer than 371 nm, which indicates high visible light transparency of the ZnO-MAA NPs in DCM. PI has an absorption peak at 385nm in Figure S6, which corresponds to the wavelength of DLP.²⁸ Therefore, high visible light transparency high and UV light absorption of ZnO-MAA NPs demonstrates preferable properties for transparent packaging materials, which is similar to the ZnO NPs made by Li *et al.*²⁹

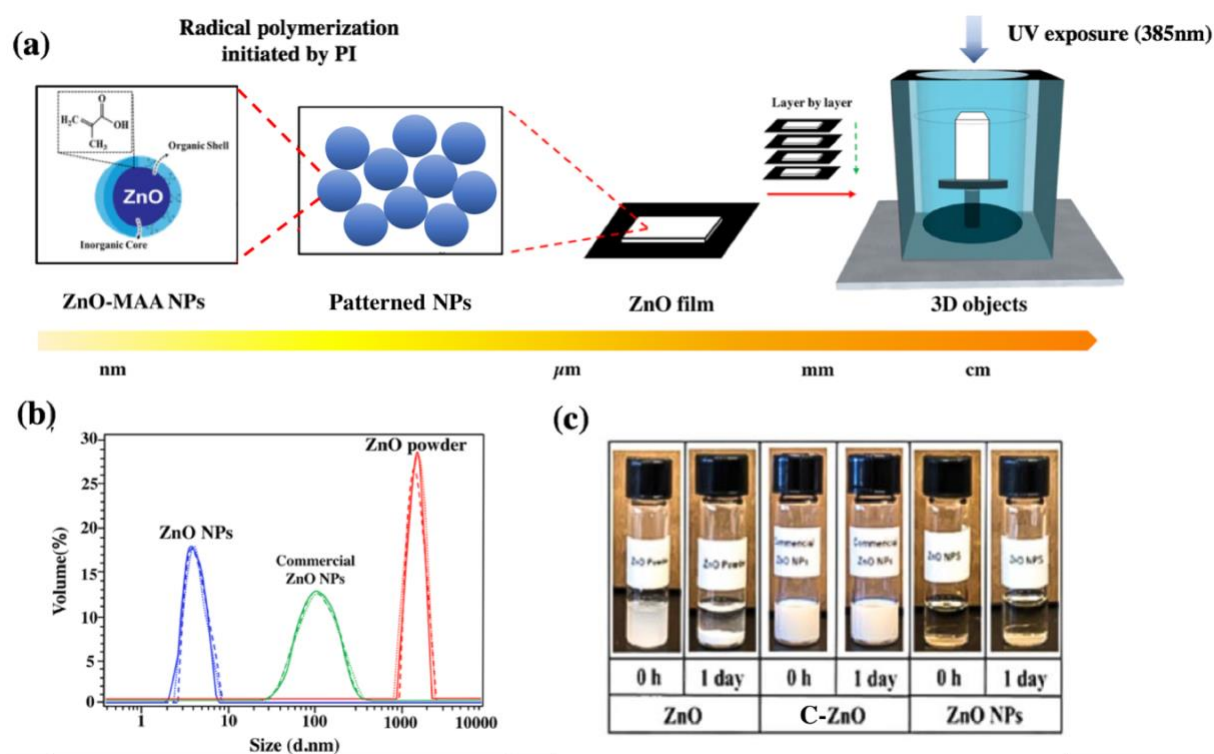


Figure 1. (a) A schematic diagram illustrating the Samples of precursor ZnO-MAA NPs that form a ZnO film. The film was built up layer-by-layer to form three-dimensional (3D) objects. (b) Particle size distributions as detected by dynamic light scattering of the ZnO powder, C-ZnO NPs and ZnO-MAA NPs dissolved in DCM. (c) Photographs of the ZnO powder, C-ZnO NPs and ZnO-MAA NPs after immersion for 0 and 1 day in dichloromethane (DCM).

7.4.2. Film properties of 3D printed ZnO layer

A UV projector was used to pattern the ZnO-MAA NPs, which were highly photosensitive (Figure S1). The wavelength of our DLP system was ca. 385 nm. The photoradical generator stripped off methacrylic acid ligands when exposed to UV light in this range. Then, the selected area under UV exposure is patterned.³⁰ Well-dispersed NPs with high photosensitivity are needed to deliver layer-by-layer deposition in 3D optical printing. Figure 2(b) shows the cured speed for each layer of a ZnO film for various light intensities (1.0–5.0 mW/cm²). The ZnO-MAA NPs and photoradical generator (10%) in DCM were added to the 3D optical printing reservoir. The curing speed for each layer was measured by dividing the height of a single layer by the exposure time. The curing speed for each layer increased initially with increasing light intensity, but then reached a steady speed after the light intensity reached 3.0 mW/cm². At

steady state, the ZnO-MAA NPs photo-cured at 3.0 mW/cm^2 illumination under N_2 and O_2 was about $2.3 \text{ }\mu\text{m/s}$ and $3.3 \text{ }\mu\text{m/s}$ (cured speed for each layer), respectively, revealing that the photo-curing rate in N_2 was higher than in O_2 due to oxygen inhibition. Higher light intensity provided faster curing speeds due to a higher number of initiated free radicals.

Figures S7(a) (b) show SEM images of each ZnO layer under UV exposure for 40 s under nitrogen. At low magnification (Figure S7(a)), the surface of the film appears smooth. At high magnification (Figure S7(b)), the ZnO-MAA NPs appear as a homogenous and uniform non-porous film. The morphology of the film and its homogeneity was studied by AFM. Figure S7(c) shows 3D topographies of an amorphous ZnO film imaged in the tapping mode. Although the film was not perfectly uniform, the height variation was less than several nanometers.

X-ray diffraction (XRD), TEM, selected area electron diffraction (SAED) patterns and energy dispersive X-ray spectroscopy (EDAX) were used to analyze the structure and constituents of the ZnO-MAA NPs and the film. The XRD patterns of the ZnO film before and after calcination at 700°C are shown in Figure 2(c). The diffraction peaks indicated that the initial film was amorphous. Cho *et al*³¹ shows the benefit amorphous ZnO film involves enables processing ZnO film in a relatively low temperature, and adapts for determining the optical constant for the material in a wide range. The amorphous result is primarily because NPs are embedded in the organic matrix. However, (100), (002), (101), (102) and (110) facets appeared after calcination at 700°C . This result is similar to that reported by Zhang *et al.*, who identified the material as the hexagonal wurtzite form of ZnO.³² Also, Aslan *et al.*³³ indicates (002) peak is the the thermodynamically preferential orientation of zinc oxide. After annealing, they reported higher intensity of (002) peak, which is attribute to the decrease in lattice parameter in c-axis and lattice deformations. TEM was used to observe the morphology of the ZnO films shown in Figure S8 (a). A smooth morphology and no long-range ordering are

evident in the cross-sectional images. Furthermore, the SAED pattern (Figure S8 (a)) shows that the 3D-printed ZnO film sample was amorphous. Figure S8 (b) shows the EDS results for a FIB-trimmed film specimen placed on a Cu grid. The film contained C, O, Zn and Cu (from the Cu grid). Additionally, the photo-radical generator was removed during the 3D printing process so that the final film was composed of just C, O and Zn.

The interface compatibility properties of the C-ZnO NPs/MAA (physically blended) and the ZnO-MAA NPs for the patterned film formation were determined by observing the surface morphology and distribution. Typical SEM-EDS micrographs for the surfaces of the C-ZnO NPs film (C-ZnO NPs/MAA physically blended) and ZnO-MAA NPs film are shown in Figure S9(a, b). The SEM-EDS micrograph of the C-ZnO NPs film in Figure S9(a) indicates that the Zn in the C-ZnO NPs was not uniformly distributed (yellow arrows indicate regions lacking elemental Zn). Poor adhesion between the C-ZnO NPs and MAA matrix was observed because a large amount of the C-ZnO NPs was not entirely covered by MAA during photopolymerization. On the other hand, the SEM-EDS micrograph of ZnO-MAA NPs in Figure S9(b) indicates better adhesion of ZnO-MAA NPs with the matrix, and Zn is homogeneously dispersed in the ZnO NPs film. Building up films by NPs leads to a more uniform distribution of Zn.

The thermal stability of a ZnO film was assessed by TGA. Figure S10 demonstrates that degradation of the ZnO film occurred in two steps. The first step starts at 150°C and is related to water or DCM in the sample. The second step spans 385–520°C and is attributed to decomposition of the organic fraction. Additionally, Figure S10 shows that the residual char from the ZnO film was 38.6% higher than from PMMA at 700°C. The thermal stabilities of the ZnO film is much better than PMMA, because the thermal degradation of the organic fraction becomes more difficult due to interfacial interactions between ZnO and the MAA ligands.

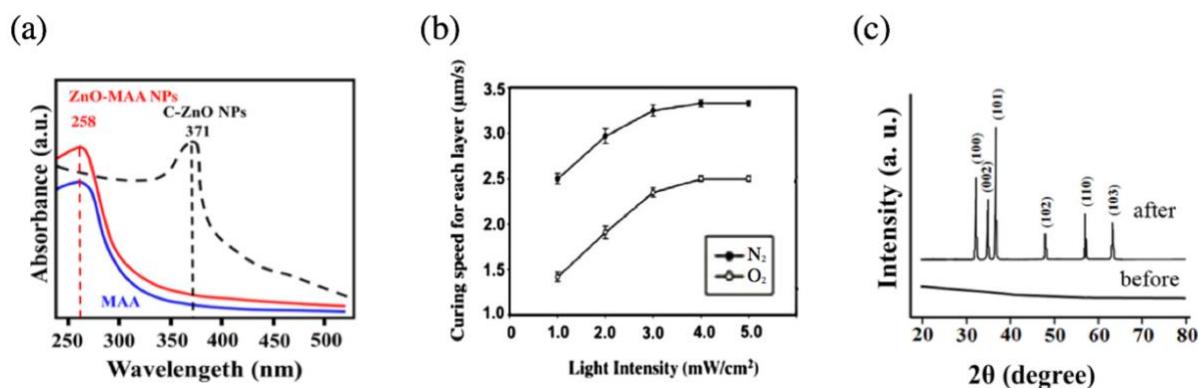


Figure 2. (a) Ultraviolet-visible (UV-Vis) absorption spectra for ZnO-MAA NPs, ZnO NPs (C-ZnO NPs) (b) Curing speed for each ZnO layer under 385-nm ultraviolet light as a function of light intensity (1.0–5.0 mW/cm²) under air and nitrogen atmospheres. (c) X-ray diffraction (XRD) patterns of the ZnO film before and after calcination at 700°C.

7.4.3. Optical projection of 3D structures

Figure 3(a) reveals monolayers of parallel lines, bent corners and a square array with voids for structures printed by the digital light processing. Several patterns were designed to assess the resolution limit. Identical patterns at different scales were printed by the DLP machine. After 3D printing, we used an optical microscope to inspect the images to judge the resolution limit. The two-dimensional (2D) optical microscopy image indicates good 2D resolution, which can reach 50 μm with straight lines and edges (the theoretical resolution is 10 μm). The resolution depends on the interaction of UV light with the NPs and the diffusion of free radicals. Figure 3(b) shows SEM images of a honeycomb, a butterfly and the Cornell logo, which were all fabricated using an optical projector at 385 nm. Although other 3D manufacturing processes can print similar objects, the optical projection method can produce objects having larger areas and with more complex structures in a shorter time compared with those techniques that require a separate mask fabrication process.³⁴

The height variation could be reduced by increasing the distance between the stage and the liquid surface. Stage movement was computer-controlled. Projecting different patterns onto the liquid surface enables the building of complex 3D items. Figure 3(c) shows several 3D

items fabricated by this technique (annotated with X, Y and Z-axis): a hollow cuboid, a pyramid and a townhouse, each one several centimeters in size.

More precise and higher energy techniques are needed to create more complex objects. Our projector design limited the penetrating thickness from the top of the liquid space to the stage. SLA could be used to print more sophisticated structures.

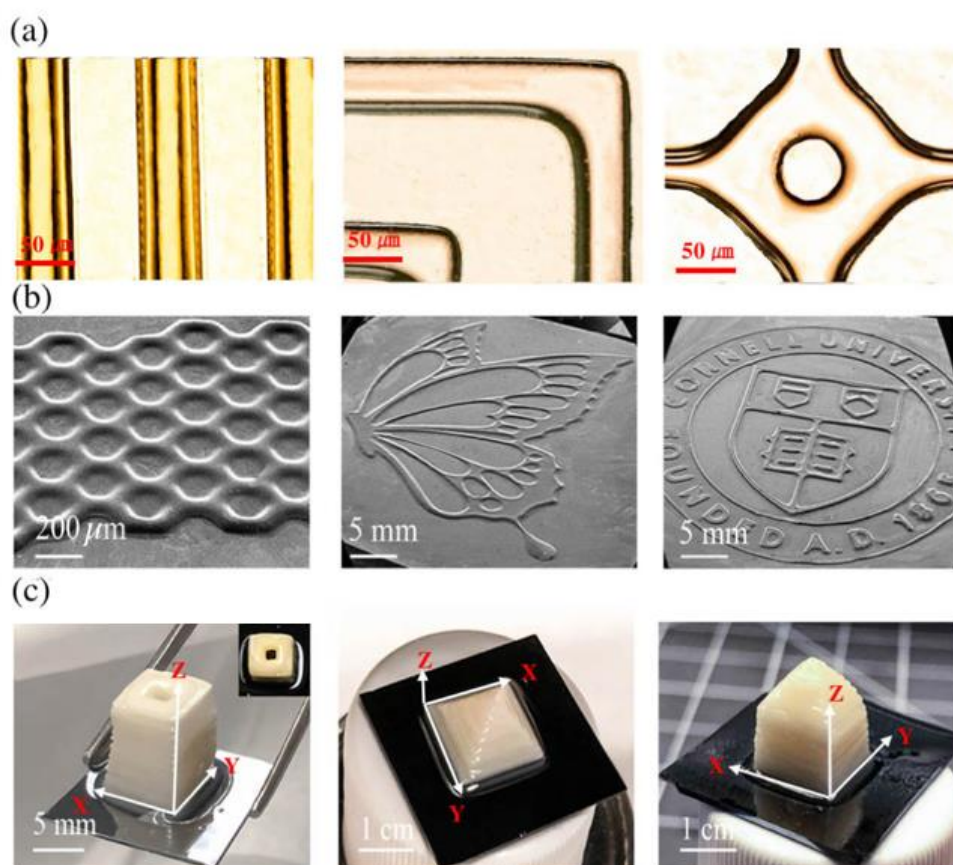


Figure 3. (a) Parallel lines, bent corners and a square array with voids. (b) Honeycomb, butterfly and Cornell logo microstructures printed by the digital light processing technique. (c) Hollow cuboid, pyramidal and townhouse 3D structures manufactured by this technique.

7.4.4. Electrical properties of 3D printed ZnO

ZnO has been reported to exhibit interesting semiconducting behavior. To demonstrate the electrical properties of ZnO film, we did transmission line measurement. The resistivity is $2.51 \times 10^4 \Omega \cdot \text{m}$ for ZnO film, which is an insulator. This result is similar to the Muchuweni *et al.*, who used spray pyrolysis method to produce ZnO thin film on glass substrate. The

resistivity of the ZnO thin film they deposited is approximately $6.03 \times 10^3 \Omega \cdot \text{m}$.³⁵ Also, Xing *et al.*³⁶ shows that before annealing the zinc oxide film prepared by magnetron sputtering is an insulator with high resistivity. In comparison, the resistivity dropped to $6.2 \times 10^1 \Omega \cdot \text{m}$ after calcination, which is close to a ZnO semiconductor.^{37, 38} This resistivity is lower than undoped ZnO film reported by Biswal *et al.*,³⁹ this can be assigned to the organic fraction of the 3D printed film was decomposed. Figure 4(a) indicates that the resistivity decreases after calcination at 700°C and XRD result confirms the characterization peaks of hexagonal wurtzite ZnO appears after the calcination in Figure S7. Figure 4(b) show the I-V characterization of 3D printed ZnO film before and after the calcination. Ohmic behavior was observed before calcination with a linear I-V curve (Figure 4 (b)). After calcination, it is worth while to note that a raise in current is observed. Figure 4 (b) show the non-ohmic curve depicts the semiconducting behavior of the 3D printed ZnO film, which is similar to the I-V curve of ZnO nanoparticle film by Gedamu *et al.*⁴⁰. As a result, 3D printed ZnO can open possibilities to making high resistivity packaging material and semiconducting devices in the near future.

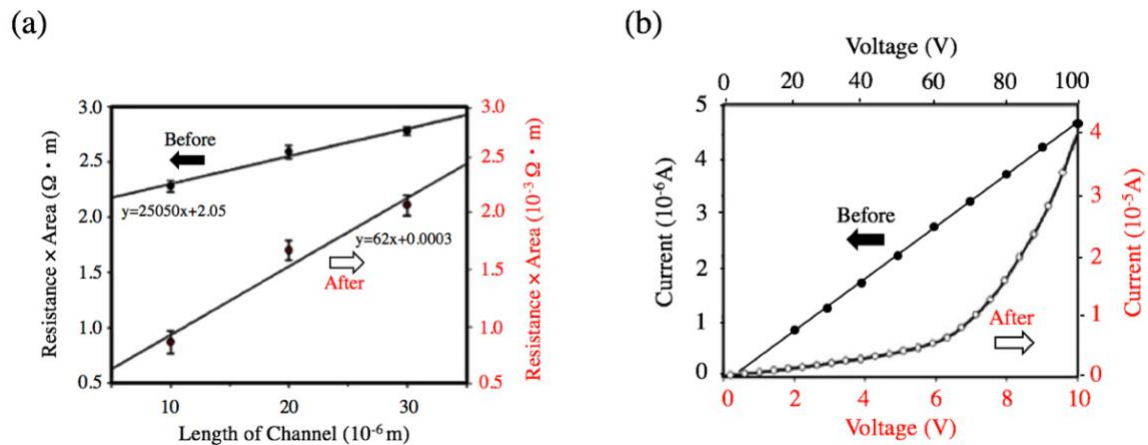


Figure 4. (a) Electrical resistivity, (b) I–V curve characteristics of ZnO film before and after calcination at 700°C.

7.5. Conclusion

To the best of our knowledge, this is the first report of ZnO-based NP ink for 3D DLP. DLS analysis confirmed that these NPs were monodispersed in DCM with a particle size of ca. 3–5 nm. They acted as building blocks that were used to construct mesoscale 3D structures, which can be more precisely programmed, based on the intermolecular connection with MAA ligands. UV light was used to initiate ligand stripping mechanism, which photocured areas selected for exposure. The limit of resolution by optical microscopy was 50 μm . The printing speed of ZnO reached 3.3 $\mu\text{m/s}$ as the intensity reached 3.0 mW/cm^2 under a nitrogen atmosphere. AFM topography imaging indicated individual layer roughness of several nanometers. SAED and XRD revealed the amorphous structure of the ZnO film. 3D printed ZnO film is a high electrical resistivity insulator. After calcination at 700°C, 3D printed ZnO film shows lower electrical resistivity and nonlinear I–V properties due to the decomposition of organic fraction. Above all, this study offers a prospective way to manufacture 3D printed ZnO macrostructures for future development of optoelectronic and semiconductor devices.

7.6. Acknowledgments

This work was performed in part at the Cornell NanoScale Facility, a member of the National Nanotechnology Coordinated Infrastructure (NNCI), which is supported by the National Science Foundation (Grant ECCS-1542081). This work made use of the Cornell Center for Materials Research Shared Facilities which are supported through the NSF MRSEC program (DMR-1719875). TH and JH acknowledge support from NSF-CMMI 1635433. We are grateful for the scientific and technical assistance from Cornell's Center for Nanomaterials Engineering and Technology. The authors gratefully acknowledge Kou Yang for helping on ZnO NPs synthesis and Dr. Richards, for preparation and assistance on transmission line measurement.

7.7. Supporting Information

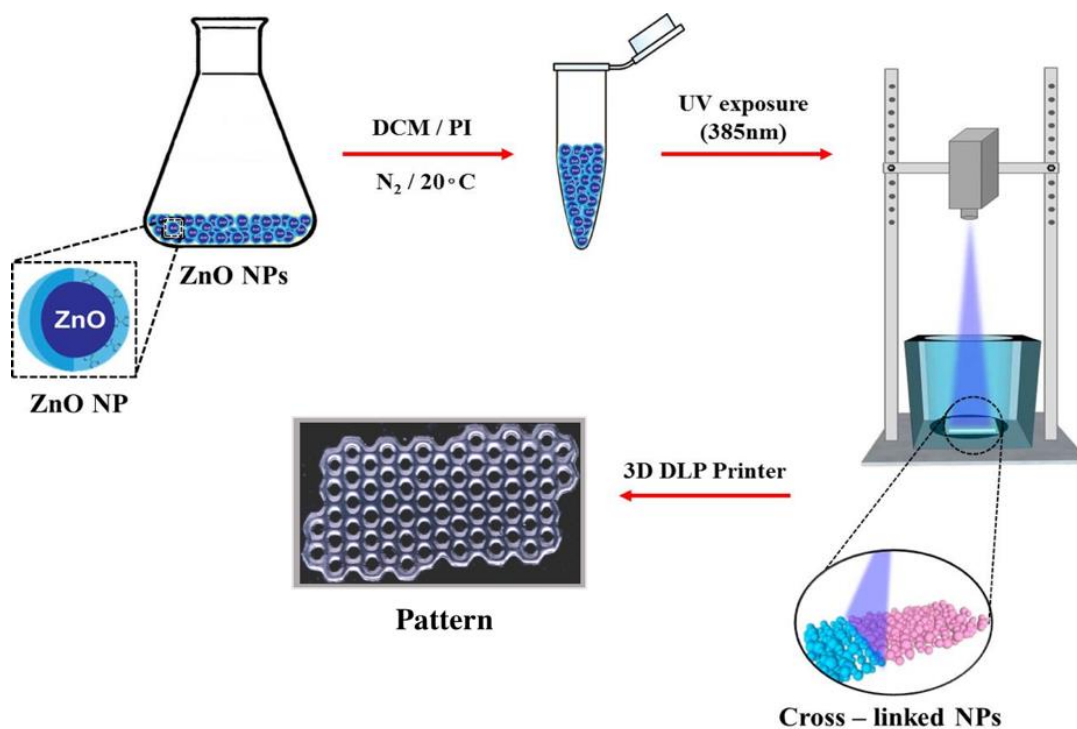


Figure S1. Fabrication of three-dimensional-printed products from photo-cured zinc oxide-methacrylic acid nanoparticles (ZnO-MAA NPs).

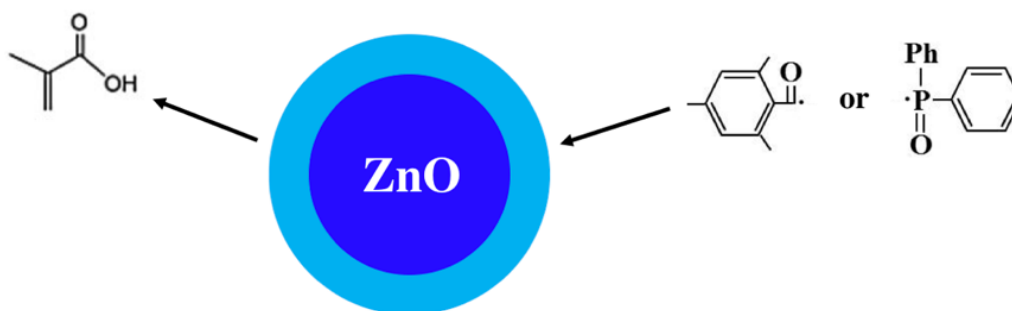
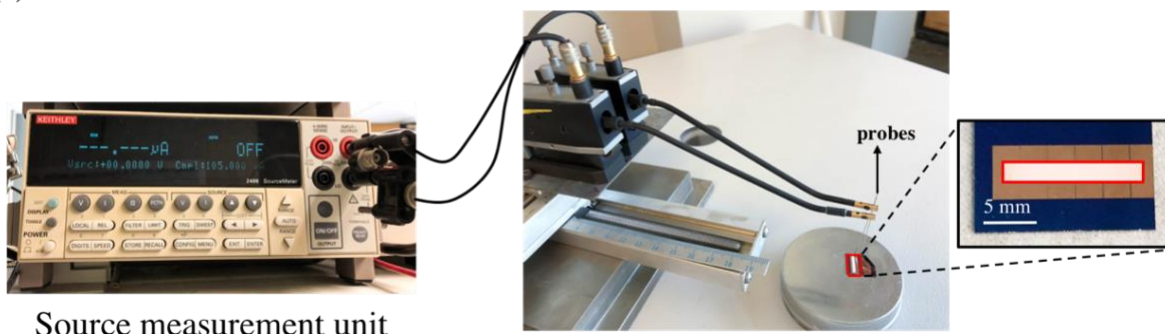


Figure S2. Possible mechanism for photosensitive ligands on inorganic core of ZnO-MAA NPs ink.

(a)



Source measurement unit

(b)

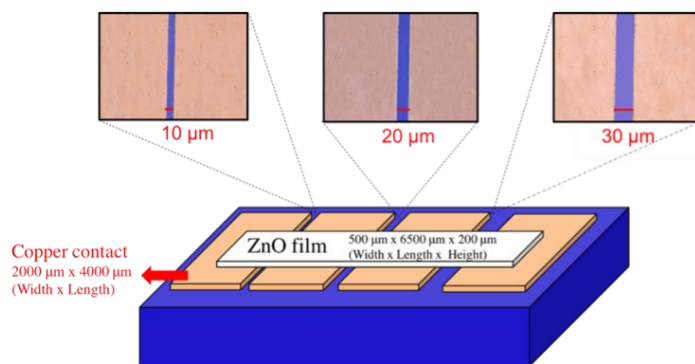


Figure S3. (a) Experimental setup of transmission line measurement; and (b) Schematic junctions of ZnO film for transmission line measurement.

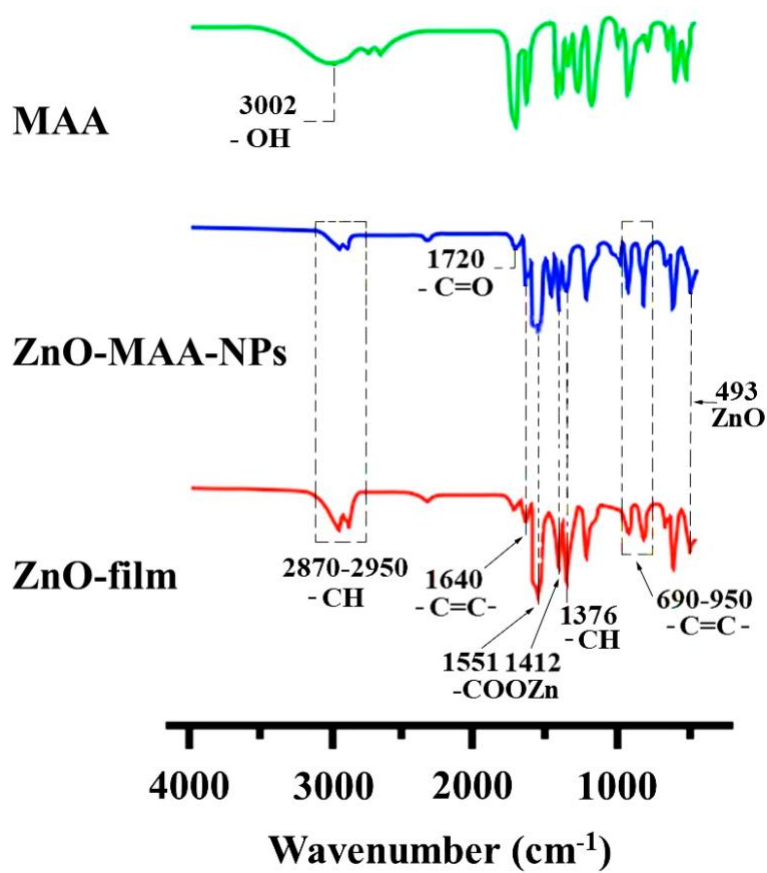


Figure S4. Fourier transform-infrared (FT-IR) spectra of methacrylic acid (MAA) zinc oxide-based nanoparticles (ZnO-MAA NPs) and zinc oxide film (ZnO-film).

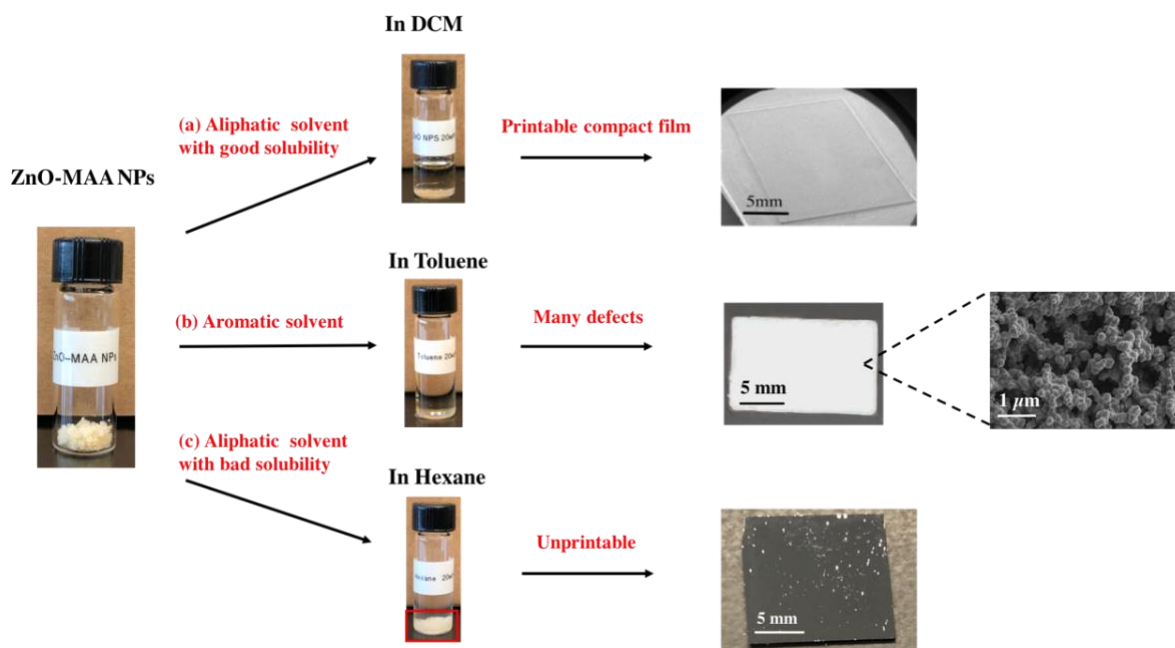


Figure S5. Comparison of printed ZnO-MAA samples in different solvent (a) DCM (b) Toluene, and (c) Hexane.

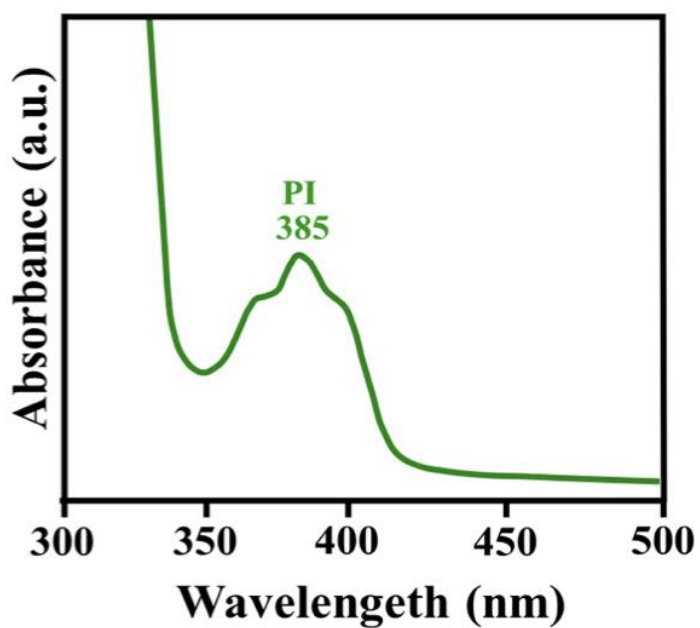


Figure S6. Ultraviolet-visible (UV-Vis) absorption spectra for PI dissolved in DCM solution.

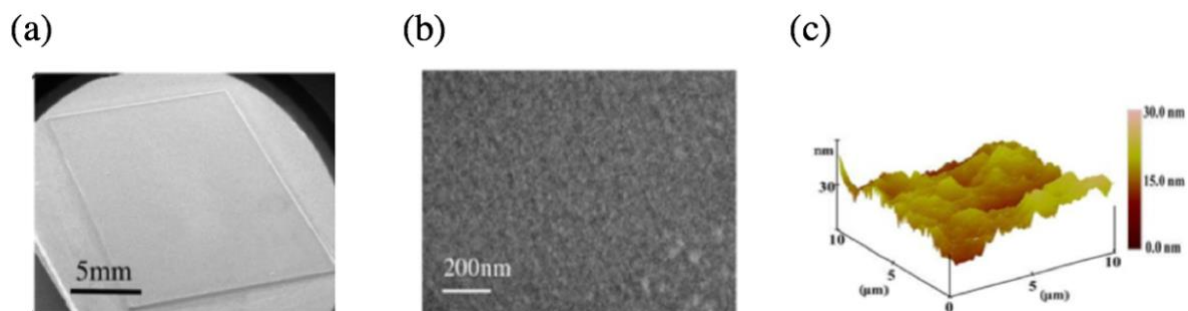


Figure S7. (a) Scanning electron microscopy (SEM) image of a layer of ZnO film photopolymerized for 40 s under a nitrogen atmosphere. (b) Scanning electron microscopy (SEM) image of a layer of ZnO film photopolymerized for 40 s under a nitrogen atmosphere. (c) Atomic force microscopy images of ZnO films showing 3D topographies (scale bar: $10\ \mu\text{m} \times 10\ \mu\text{m} \times 30\ \text{nm}$).

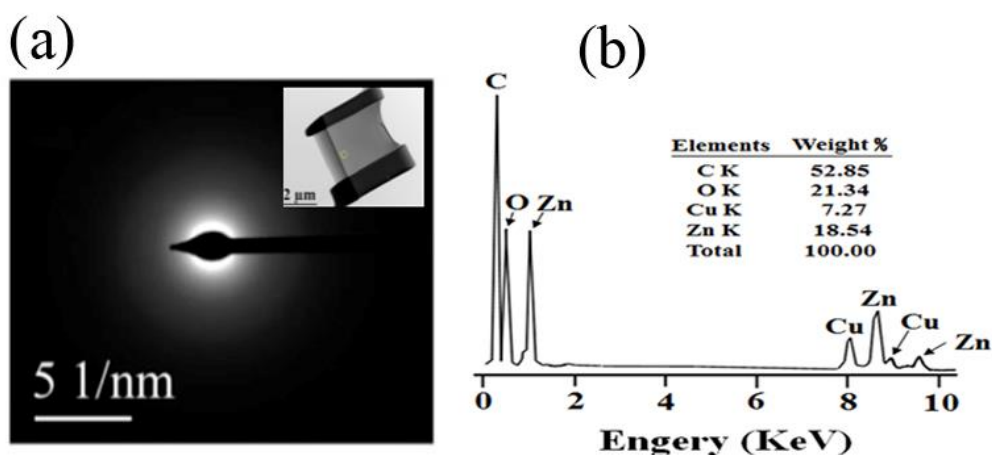


Figure S8. (a) Selected area electron diffraction patterns (SAED) ZnO film (focused ion beam (FIB) pattern) and transmission electron microscopy (TEM) image of ZnO film; and (b) Quantitative energy dispersive spectroscopy (EDS) analysis of a ZnO film.

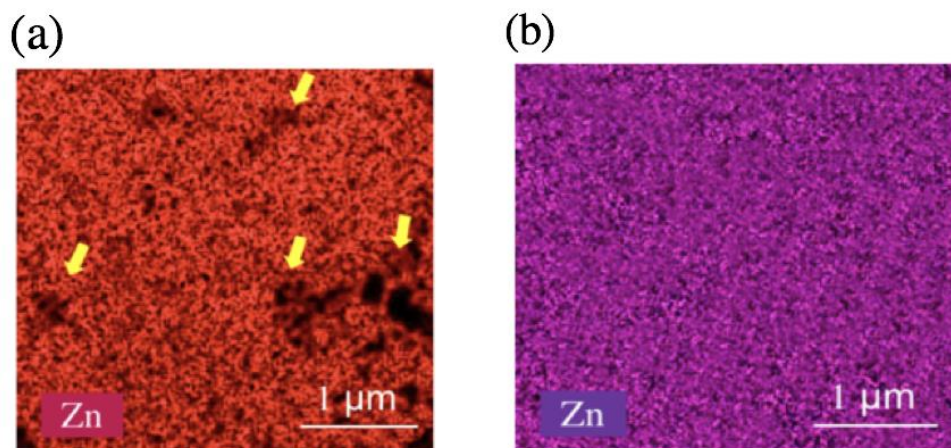


Figure S9 (a) and (b) SEM-energy dispersive spectroscopy analysis of a C-ZnO NPs/MAA (physically blended) film and a ZnO-MAA NPs film formed by photopolymerization.

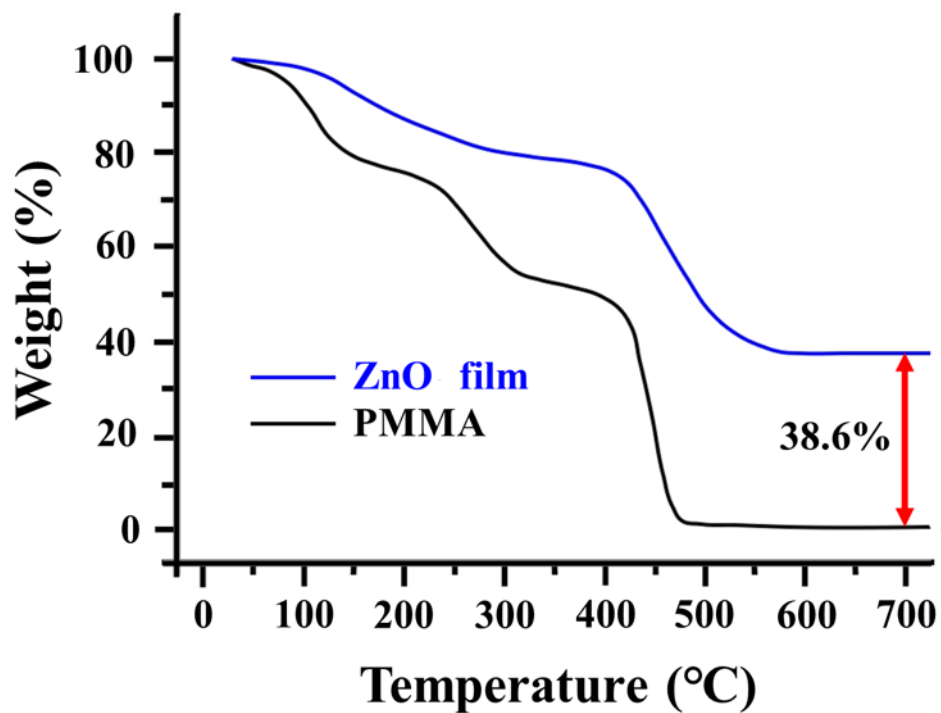


Figure S10. Thermogravimetric analysis (TGA) curves for PMMA and ZnO film.

7.8. References

- (1) Noorani, R., 3D Printing: Technology, Applications, and Selection. CRC Press; Taylor & Francis Group Co. Pte. Ltd., 2017.
- (2) Lipson, H.; Kurman, M., Fabricated: The New World of 3D Printing, 1st Ed.; Wiley Co. Pte. Ltd., 2013.
- (3) Mironov, V.; Boland, T.; Trusk, T.; Forgacs, G.; Markwald, R. R., Organ printing: computer-aided jet-based 3D tissue engineering. *Trends Biotechnol.* 2003, *21* (4), 157-161.
- (4) Sun, K.; Wei, T.-S.; Ahn, B. Y.; Seo, J. Y.; Dillon, S. J.; Lewis, J. A., 3D Printing of Interdigitated Li-Ion Microbattery Architectures. *Adv. Mater.* 2013, *25* (33), 4539–4543.
- (5) Kong, Y. L.; Tamargo, I. A.; Kim, H.; Johnson, B. N.; Gupta, M. K.; Koh, T.-W.; Chin, H.-A.; Steingart, D. A.; Rand, B. P.; McAlpine Michael, C., 3D Printed Quantum Dot Light-Emitting Diodes. *Nano Lett.* 2014, *14* (12), 7017-7023.
- (6) MacDonald, E.; Salas, R.; Espalin, D.; Perez, M.; Aguilera, E.; Muse, D.; Wicker, R. B., 3D Printing for the Rapid Prototyping of Structural Electronics. *Access, IEEE* 2014, *2*, 234-242.
- (7) Ligon, S. C.; Liska, R.; Stampfl, J.; Gurr, M.; Mulhaupt, R. Polymers for 3D Printing and Customized Additive Manufacturing. *Chem. Rev.* 2017, *117*(15), 10212–10290.
- (8) Castro, N. J.; Hutmacher, D. W. Designification of Neurotechnological Devices through 3D Printed Functional Materials. *Adv. Funct. Mater.* 2018, *28*(12), 1703905.
- (9) Chen, X.; Liu, L.; Feng, Y.; Wang, L.; Bian, Z.; Li, H.; Wang, Z. L. Fluid eddy induced piezo-promoted photodegradation of organic dye pollutants in wastewater on ZnO nanorod arrays/3D Ni foam. *Mater. Today* 2017, *20*(9), 501–509.

- (10) Xue, X.; Zang, W.; Deng, P.; Wang, Q.; Xing, L.; Zhang, Y.; Wang, Z. L. Piezo-potential enhanced photocatalytic degradation of organic dye using ZnO nanowires. *Nano Energy* 2015, *13*, 414–422.
- (11) Liang, Y. N.; Lok, B. K.; Wang, L.; Feng, C.; Lu, A. C. W.; Mei, T.; Hu, X. Effects of the morphology of inkjet printed zinc oxide (ZnO) on thin film transistor performance and seeded ZnO nanorod growth. *Thin Solid Films* 2013, *544*, 509–514.
- (12) Assaifan, A. K.; Lloyd, J. S.; Samavat, S.; Deganello, D.; Stanton, R. J.; Teng, K. S. Nanotextured Surface on Flexographic Printed ZnO Thin Films for Low-Cost Non-Faradaic Biosensors. *ACS Appl. Mater. Interfaces* 2016, *8*(49), 33802–33810.
- (13) Gedamu, D.; Paulowicz, I.; Kaps, S.; Lupan, O.; Wille, S.; Haidarschin, G.; Mishra, Y. K.; Adelung, R. Rapid Fabrication Technique for Interpenetrated ZnO Nanotetrapod Networks for Fast UV Sensors. *Adv. Mater.* 2014, *26*(10), 1541–1550.
- (14) Huang, J.; Yin, Z. G.; Zheng, Q. D. Applications of ZnO in Organic and Hybrid Solar Cells. *Energy Environ. Sci.* 2011, *4*, 3861–3887.
- (15) Li, Y.; Fu, J.; Zhong, C.; Wu, T.; Chen, Z.; Hu, W.; Amine, K.; Lu, J. *Adv. Energy Mater.* 2019, *9*, 1802605.
- (16) Wei, J.; Pećanac, G.; Malzbender, J. Review of mechanical characterization methods for ceramics used in energy technologies. *Ceram. Int.* 2014, *40*, 15371–15380.
- (17) Eckel, Z. C.; Zhou, C.; Martin, J. H.; Jacobsen, A. J.; Carter, W. B.; Schaedler, T. A. Additive manufacturing of polymer-derived ceramics. *Science* 2016, *351*(6268), 58–62.
- (18) Tubío, C. R.; Guitián, F.; Gil, A. Fabrication of ZnO periodic structures by 3D printing. *J. Eur. Ceram. Soc.* 2016, *36*, 3409–3415.
- (19) Torrado, A. R.; Shemelya, C. M.; English, J. D.; Lin, Y.; Wicker, R. B.; Roberson, D. A. Characterizing the effect of additives to ABS on the mechanical property anisotropy of specimens fabricated by material extrusion 3D printing. *Addit. Manuf.* 2015, *6*, 16–29.

- (20) Yu, M., Xu, H., Kosma, V., Odent, J., Kasahara, K., Giannelis, E. & Ober, C. Positive Tone Nanoparticle Photoresists: New Insight on the Patterning Mechanism. *J. Photopolym. Sci. Technol.* 2016, 29 (3), 509–512.
- (21) Tumbleston, J.R.; Shirvanyants, D.; Ermoshkin, N.; Januszewicz, R.; Johnson, A. R.; Kelly, D.; Chen, K.; Pinschmidt, R.; Rolland, J. P.; Ermoshkin, A.; Samulski, E. T. ; DeSimone, J. M. Continuous Liquid Interface Production of 3D Objects. *Science* 2015, 347 (6228), 1349–1352.
- (22) Kryask M., Trikeriotis M., Ouyang C., Chakrabarty S., Giannelis E. P., Ober, C. K. Nanoparticle Photoresists: Ligand Exchange as a New, Sensitive EUV Patterning Mechanism TI. *J. Photopolym. Sci. Technol.* 2013, 26 (5), 659–664.
- (23) Xu H., Gao J., Jiang D. Stable, crystalline, porous, covalent organic frameworks as a platform for chiral organocatalysts. *Nat. Chem.* 2015, 7(11), 905–912.
- (24) Xu, H.; Yang, K.; Sakai, K.; Kosma, V.; Kasahara, K.; Giannelis, E. P.; Ober, C. K. EUV metal oxide hybrid photoresists: ultra-small structures for high-resolution patterning. *Proc. SPIE* 2018, 10583, 105831P1-6.
- (25) Zhang, L.; Li, F.; Chen, Y.; Wang, X. Synthesis of transparent ZnO/PMMA nanocomposite films through free-radical copolymerization of asymmetric zinc methacrylate acetate and in-situ thermal decomposition. *J. Lumin.* 2011, 131, 1701–1706.
- (26) Simsikova, M.; Antalík, M., Kanuchovad, M.; Skvarla, J. Cytochrome c conjugated to ZnO–MAA nanoparticles: The study of interaction and influence on protein structure. *Int. J. Biol. Macromol.* 2013, 59, 235– 241.
- (27) Milosavljevic, N. B.; Ristic, M. D.; Peric-Grujic, A. A.; Filipovi c, J. M.; Strbac, S. B.; Rakocevic, Z. L.; Krusic, M. T. K. Sorption of zinc by novel pH-sensitive hydrogels based on chitosan, itaconic acid and methacrylic acid. *J. Hazard. Mater.* 2011, 192, 846–854.

- (28) Pawar, A. A.; Saada, G.; Cooperstein, I.; Larush, L.; Jackman, J. A.; Tabaei, Seyed R.; Cho, N. J.; Magdassi, S. High-performance 3D printing of hydrogels by water-dispersible photoinitiator nanoparticles. *Sci. Adv.* 2016, 2 (4), e1501381.
- (29) Li, Y. Q.; Fu, S. Y.; Mai, Y. W. Preparation and characterization of transparent ZnO/epoxy nanocomposites with high-UV shielding efficiency. *Polymer* 2006, 47 (6), 2127–2132.
- (30) Pawar, A. A.; Halivni, S.; Waiskopf, N.; Ben-Shahar, Y.; Soreni-Harari, M.; Bergbreiter, S.; Banin, U.; Magdassi, S. Rapid Three-Dimensional Printing in Water Using Semiconductor–Metal Hybrid Nanoparticles as Photoinitiators. *Nano Lett.* 2017, 17(7), 4497–4501.
- (31) Cho, D. Y.; Kim, J. H.; Na, K. D.; Song, J.; Hwang, C. S.; Park, B. G.; Kim, J. Y.; Min, C. H.; Oh, S. J. Spectroscopic evidence for limited carrier hopping interaction in amorphous ZnO thin film. *Appl. Phys. Lett.* 2009, 95 (26):261903 - 261903-3.
- (32) Zhang, Y.; Zhuang, S.; Xu, X.; Hu, J. Transparent and UV-shielding ZnO@PMMA nanocomposite films. *Opt. Mater.* 2013, 36, 169–172.
- (33) Aslan, M.H.; Oral, A.Y.; Mensur, E.; Gul, A.; Basaran, E., Preparation of c-axis-oriented zinc-oxide thin films and the study of their microstructure and optical properties. *Solar Energy Mater. Solar Cells* 2004, 82 (4), 543–552.
- (34) Kim, K.; Zhu, W.; Qu, X.; Aaronson, C.; McCall, W. R.; Chen, S.; Sirbully, D. J. 3D Optical Printing of Piezoelectric Nanoparticle Polymer Composite Materials. *ACS Nano* 2014, 8 (10), 9799–9806.
- (35) Muchuweni, E.; Sathiaraj, T. S.; Nyakoty H. Synthesis and characterization of zinc oxide thin films for optoelectronic applications. *Heliyon* 2017, 3, e00285.

- (36) Xing, G. Z.; Yao, B.; Cong, C. X.; Yang, T.; Xie, Y. P.; Li, B. H.; Shen, D. Z., Effect of annealing on conductivity behavior of undoped zinc oxide prepared by rf magnetron sputtering. *J. Alloys Compd.* 2008, 457 (1-2), 36–41.
- (37) Miller, P. H. The Electrical Conductivity of Zinc Oxide. *Phys. Rev.* 1941, 60, 890-895.
- (38) Raimondi, D. L.; Kay, E. High Resistivity Transparent ZnO Thin Films. *J. Vac. Sci. Technol.* 1970, 7, 96-99.
- (39) Biswal, R.; Castañeda, L.; Moctezuma, R.; Vega-Pérez, J.; Olvera, M. D. L. L. Maldonado, A. Formation of Indium-Doped Zinc Oxide Thin Films Using Ultrasonic Spray Pyrolysis: The Importance of the Water Content in the Aerosol Solution and the Substrate Temperature for Enhancing Electrical Transport. *Materials* 2012, 5(3), 432-442.
- (40) Gedamu, D.; Paulowicz, I.; Kaps, S.; Lupan, O.; Wille, S.; Haidarschin, G.; Mishra, Y. K.; Adelung, R. Rapid Fabrication Technique for Interpenetrated ZnO Nanotetrapod Networks for Fast UV Sensors. *Adv. Mater.* 2014, 26(10), 1541–1550.

8. SUMMARY AND OUTLOOK

This thesis concentrated on two primary topics. First, the use of mini-emulsion ARGET-ATRP to synthesize well-defined HNPs was described in detail. Second, the 3D printing of OIHN building blocks to produce mesoscale electronic structures was developed.

In Chapter 1, HNPs with tailorable canopy sizes and graft density were synthesized by combining mini-emulsion and ARGET-ATRP. The phase transfer agent, TBAB, was found to successfully assist in the transfer of monomer from the aqueous phase into micelles without the aid of acetone, marking an improvement over previous mini-emulsion ARGET-ATRP systems.

Well-defined HNPs can function as building blocks for 2D arrays and 3D superlattices by simultaneously controlling the degree of entanglement and interaction between the nanoparticle coronas (**Figure 1**). In the future, HNP cores can be replaced by different inorganic materials with desirable properties, such as high magnetization or UV absorptivity. The combination of regular 2D/3D structures and novel core materials will pave the way for a number of far-reaching applications, including mid-wave IR (MWIR) optics, Faraday rotators, flexible electronics, and bio-sensors.

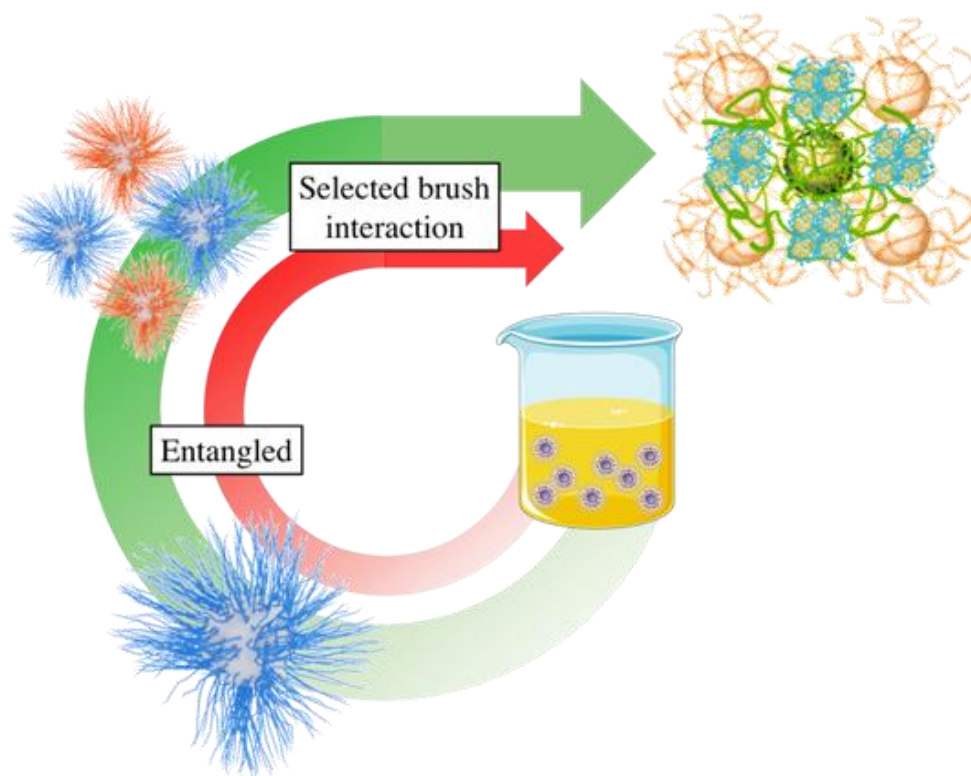


Figure 1. HNPs were prepared with appropriate graft density and specific size. By controlling the entanglement and selecting the interaction between particles, 2D arrays and superlattices can be formed.

In Chapter 2, zinc oxide nanoparticles modified by a methacrylic acid (MAA) ligand in the presence of a photoinitiator were used as building blocks to construct complex mesoscale structures (Figure 2). 3D structures exhibiting electronic properties and features as small as 50 μm were fabricated using Digital Light Processing (DLP) with a 254 nm light source. In the future, a lower weight composition of organic material in the OIHN system will allow for finer metal oxide structures with less shrinkage due to calcination. Since most of the inks available today are purely polymer-based, this work expands the materials available to DLP for applications such as high resistivity packaging and semiconductor devices. In future work, different nanoparticle cores and photosensitive ligands can be investigated to impart

useful photovoltaic, thermosensitive, mechanical, and optical properties to products produced with DLP.

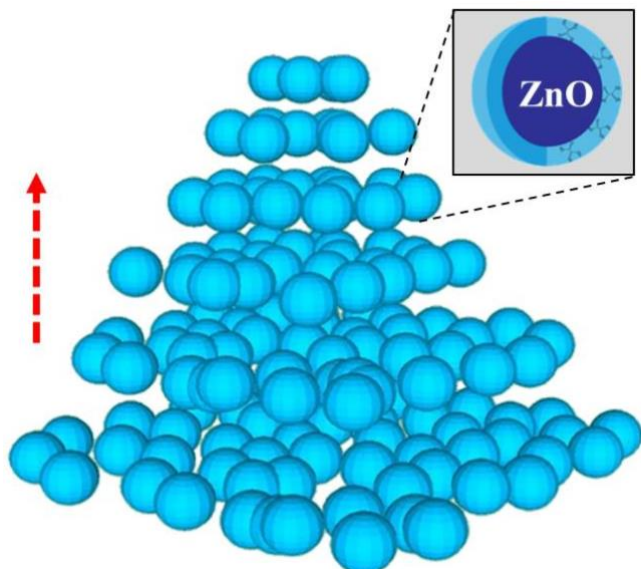


Figure 2. Zinc oxide nanoparticles modified with photosensitive ligands were used as building blocks for scaling-up complex 3D structures.